RICE UNIVERSITY

Numerical Simulations of Radiative Shocked Clumps: Application to the Young Stellar Outflow HH 29

By

Jacob Nordin Palmer

A THESIS SUBMITTED
IN PARTIAL FULFILLMENT OF THE
REQUIREMENTS FOR THE DEGREE

Master of Science

APPROVED, THESIS COMMITTEE:

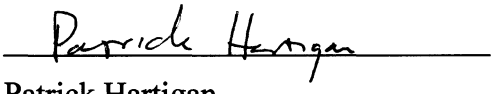

Patrick Hartigan
Professor of Physics and Astronomy
Thesis Director

Frank R. Toffoletto
Professor of Physics and Astronomy

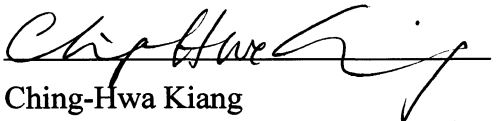

Ching-Hwa Kiang
Associate Professor of Physics and Astronomy and Bioengineering

HOUSTON, TEXAS
JULY 2011

ABSTRACT

Numerical Simulations of Radiative Shocked Clumps:

Application to the Young Stellar Outflow HH 29

by

Jacob Nordin Palmer

Herbig-Haro objects are the nebulous emission regions arising from shocks associated with the bipolar outflows of young stellar objects. Observations of the emission lines of HH objects can reveal properties of these stellar jets, which are associated with star formation, and one tool to study stellar jets and HH objects is computer modeling.

AstroBEAR is a 3D magnetohydrodynamic code with adaptive mesh refinement and parallelization capabilities. The goals of this research were (1) to improve the cooling in AstroBEAR and add the ability to create valid emission-line maps for HH objects, and (2) to model a jet overrunning and shocking clumps, and to explore a parameter space that may lead to morphologies like those of HH 29. The results generate emission-line maps with the correct spatial morphology in Hα and [SII], and begin to map out the regimes (shock velocities, resolution, physical scales) in which the code remains valid.

Table of Contents

List of Figures

List of Tables

Chapter 1
INTRODUCTION

1.1 Motivation

Astrophysical jets and outflows are found in a wide range of situations, including active galactic nuclei (Kellerman, et al. 2004), X-ray binaries (Fender, et al. 2004), and young stellar objects (Reipurth and Bally 2001). The research in this paper deals specifically with stellar jets, but it could be possible to draw parallels with other types of jets. Stellar jets are intrinsically linked to star formation, and over 600 Herbig-Haro objects (emission regions associated with the jets) had been found by 2001 (Reipurth and Bally 2001). Understanding these jets is clearly of great importance; attempts to do so go beyond direct observations, and include computer modeling and laboratory laser experiments.

Stellar jets can also be studied in a laboratory setting. Laboratory laser experiments are in the high energy density regime, far from the low density, non-LTE (Local Thermodynamic Equilibrium), optically thin regime of stellar jets. Fortunately, properly set-up experiments will scale in such a way that the dynamics can be compared with astronomical observations. Experiments of lasers into foam, for example, can recreate surprisingly similar images to some HH objects (e.g., (Hartigan et al. 2009)). While the research presented here does not focus on the laboratory aspect, it is important to note the similarities, and some examples will be presented in Chapter 5.

Many different codes have been used to model stellar jets and HH objects (for some examples, see (Tsinganos et al. 2009). An ideal code would be a 3D

Magnetohydrodynamic (MHD) code with adaptive mesh refinement (AMR) and parallelization capabilities, with proper radiative cooling and the ability to create valid emission line maps, and with the ability to also model laboratory experiments. Many 3D parallel codes with AMR capabilities exist, some of which also predict emissions lines. These codes, however, tend to use simplified parameterized fits for cooling (e.g. Raga et al. 2002). The modified AstroBEAR code described in this thesis is particularly well suited for modeling HH objects through its successful inclusion of the non-LTE forbidden line cooling needed to provide the direct connection to observations via synthetic emission line maps. This thesis will present simulations of stellar jets that shock against slower stellar outflow material and dense clumps, in the manner of HH objects, and will demonstrate the validity of AstroBEAR's cooling and emission line maps. In addition, I will model HH 29 and attempt to constrain some of its parameters.

1.2 Stellar Jets and Herbig-Haro Objects

Herbig-Haro (HH) objects are nebulous objects associated with star formation and young stars. First observed by Herbig (Herbig 1950; Herbig 1951) and Haro (Haro 1952; Haro 1953), HH objects are now believed to be related to the jets of gas emitted along the poles of rotating young stellar objects (Reipurth and Bally 2001). This outflow gas is supersonic relative to the interstellar medium (ISM) and creates a bow shock at its leading edge. The shock excites and ionizes the gas, which then cools and emits radiation at distinct frequencies.

Stellar jets are an intrinsic part of star formation, yet the details of their launch mechanism are still unclear; however, stellar jets are associated only with stars that have accretion disks, and it appears that the jets are powered by the release of gravitational energy that accompanies accretion (Reipurth and Bally 2001). Jets help to carry off excess angular momentum from the accretion process. There are competing theories about what actually launches the jet, though they all involve magnetohydrodynamic processes and magnetic field lines anchored to the spinning disk (Ferreira et al. 2006; Shang et al. 2007). The main theories are those of the X-wind and the extended disk wind. In the X-wind theory the jet is launched from within about 10 stellar radii, and interacting with the inner boundary of the disk (Shu et al. 2000), whereas in the disk-wind theory the jet is launched from an extended region farther out in the disk, at approximately 0.1- 3 AU from the star (Cabrit et al. 2005; Pudritz et al. 2007).

Observations of HH objects show that stellar jets are often highly collimated, yet that collimation does not happen at the launch site, where opening angle is wider. As with the launch mechanism, the process that collimates the jets probably involves magnetic fields. The collimation process occurs at around 10 AU or more from the star (Reipurth and Bally 2001).

The speeds of stellar jets are typically in the hundreds of km/s, yet the emission from excitation lines often indicates that the shock speeds are only tens of km/s. There were early difficulties reconciling these observed low excitation spectra with the known high velocities of the jets. Two possibilities were a) oblique shocks, which result in reduced shock velocities (see section 2.1 for a brief discussion of oblique shocks), and b) variable velocities. This second option suggests that there are internal velocity

differences within the jet, causing faster material to overtake and shock against slower material, but with a shock speed much lower than the bulk jet speed. This latter case seems to apply to HH 29, discussed below in section 1.3, and is generally favored due to observations of the proper motions of clumpy knots within the jets.

Often there are multiple HH objects associated with a given star, an indication of larger scale time varying jet velocities; as with the clumpy knots, if faster jet material runs into earlier slower jet material, it creates a shock that is then seen as a separate HH object associated with the outflow. Typical young stellar outflows have speeds of roughly 100-1000 km/s, lengths of 0.1 – 20 pcs, and ages of $10^3 - 10^6$ years (Bally and Reipurth 2002). These speeds and ages indicate that the leading bow shock of the jet would have traveled far enough and be diffuse enough that we would not observe it. The HH objects we do observe are therefore subsequent bows, caused by faster jet material shocking against slower, previously shocked jet material.

It is quite possible that magnetic fields are present in the jets themselves (or in the material through which the jets travel). Observationally, however, the presence and strength of magnetic fields are difficult to determine, as it is hard to distinguish between emission from magnetic shocks and the emission of non-magnetic lower velocity shocks. The effect of a magnetic field (with some nonzero component perpendicular to the direction of the jet flow) is to inhibit post-shock compression due to cooling. The magnetic field strength $B \sim n$ in the cooling zone of a shock, where n is the density, and the gas pressure P_{Gas} is roughly constant in that region; it follows that the magnetic field strength goes as the inverse temperature ($B \sim T^{-1}$), and the magnetic pressure goes as the

magnetic field strength squared ($P_B \sim B^2$), so $P_B/P_{Gas} \sim T^{-2}$. These two pressures can become equivalent in cooling zones as the temperature drops (Hartigan 2003).

In the case of HH objects, the regime is far from being in local thermodynamic equilibrium (LTE), and the object is optically thin to its emission. This means that we can see everything it emits, providing us with a global picture of HH objects.

1.3 HH 29

HH 29 is located in the Lynds L1551 dark cloud, at a distance of approximately 140 pc from us (Elias 1978). Originally it appeared that HH 29 was associated with the outflow from the young star L1551-IRS5. This was due largely to the direction of HH 29's bow shock, which points away from IRS5, combined with the lack of any other known potential source star in the region (Devine et al. 1999). L1551-NE, a deeply embedded low-luminosity class 0 protostar, was later discovered (Emerson et al. 1984) approximately 0.19 pc from HH 29 (~5' on the sky). A study of the proper motions of HH 29 in both Hα and [SII] concluded that L1551-NE was a more likely source for HH 29 (Devine et al. 1999) (see Figure 1). A further study of the region in [FeII] also concluded that L1551-NE was the source of HH 29 (Reipurth et al. 2000).

The proximity and brightness of HH 29 have allowed for detailed studies of its properties. Combining radial velocities from line widths with bow shock models, (Stocke et al. 1988), determined an orientation angle of 47° toward us. This predicted a proper motion of 145 km/s, which agrees with the 150 km/s measured by (Cudworth and Herbig 1979). The shock velocity, as determined from line widths, is as high as 190 km/s at the

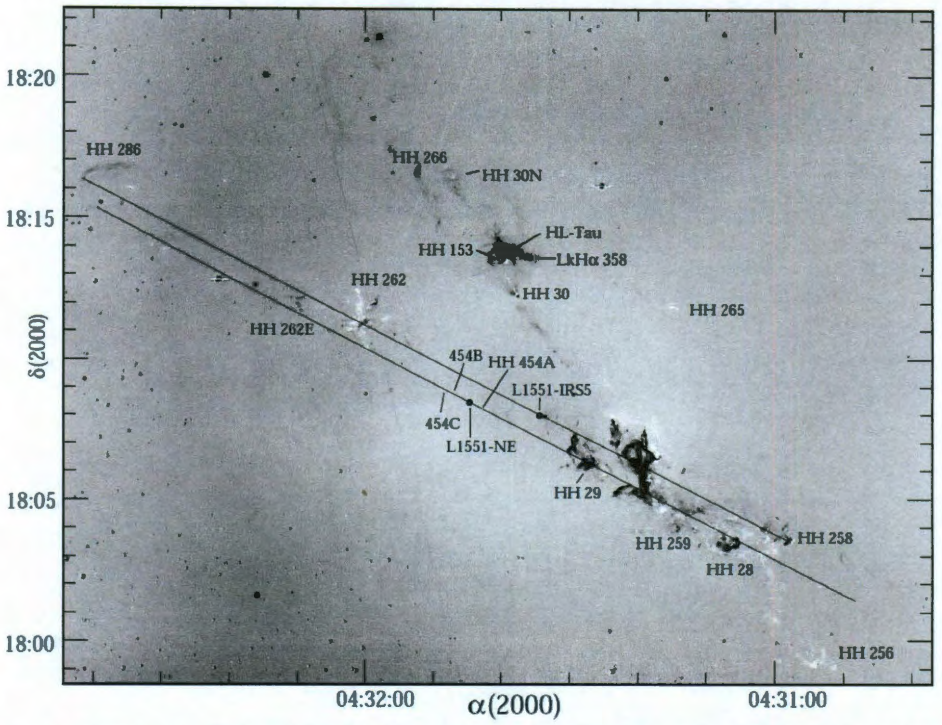

Figure 1: Lynds cloud L1551, showing HH 29 and the line of the outflow connecting it to its source star, L1551-NE. The region is complicated by the presence of multiple young stars and many HH objects. (Devine et al. 1999)

apex of the bow shock (Stocke et al. 1988). Fridlund et al. 1993 put the shock velocity at 90 ± 10 km/s based on the bow shock models of Hartigan et al. 1987. This much lower value may be due to averaging out the shock velocities of the apex and the wings of the bow shock; the material in the wings hits the ambient material at an angle, resulting in a lower shock velocity (Hartigan et al. 1987) (Figure 6). Due to the presence of [OIII] lines in HH 29, it is known that the shock velocity must be greater than ~80 km/s, since [OIII] requires the higher post-shock temperatures found in these higher velocity shocks (Fridlund et al. 1993).

HH 29 is not the leading bow shock of this outflow. If its bulk velocity has been approximately constant over its lifetime, then at a proper motion of 150 km/s and a distance of 0.19 pc from its source, it has been travelling for approximately 1200 years.

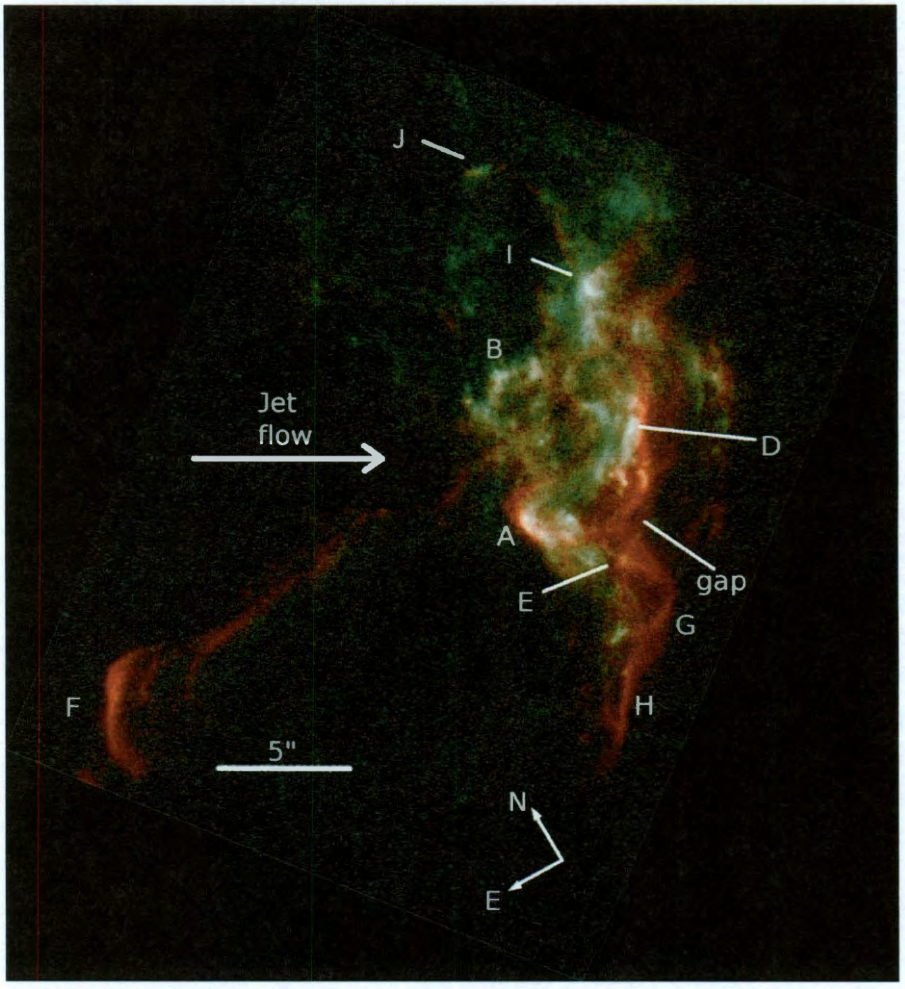

Figure 2: HST image of HH29. Hα is in red and [SII] is in green and blue. The letters indicate possible clumps. The shock is being driven to the right (and 45° toward us) by the jet. The scale of 5" corresponds to 720 AU. (Devine et al., 2000)

This is much shorter than the lifetime of the protostar, meaning the leading bow of the outflow is well beyond HH 29.

Several very distinct features are observed in HH 29. Devine et al., 2000, took high resolution HST images of the object in Hα and [SII], which provide the best detailed optical observation of HH 29 (see Figure 2). Other valuable information regarding the kinematics of HH 29 comes from images taken by (Hartigan et al. 2000) on a Fabry-Perot spectrometer, which allowed them to view Hα and [SII] at different radial velocities and create a radial velocity map of the emissions, shown here in Figure 3. Devine et. al,

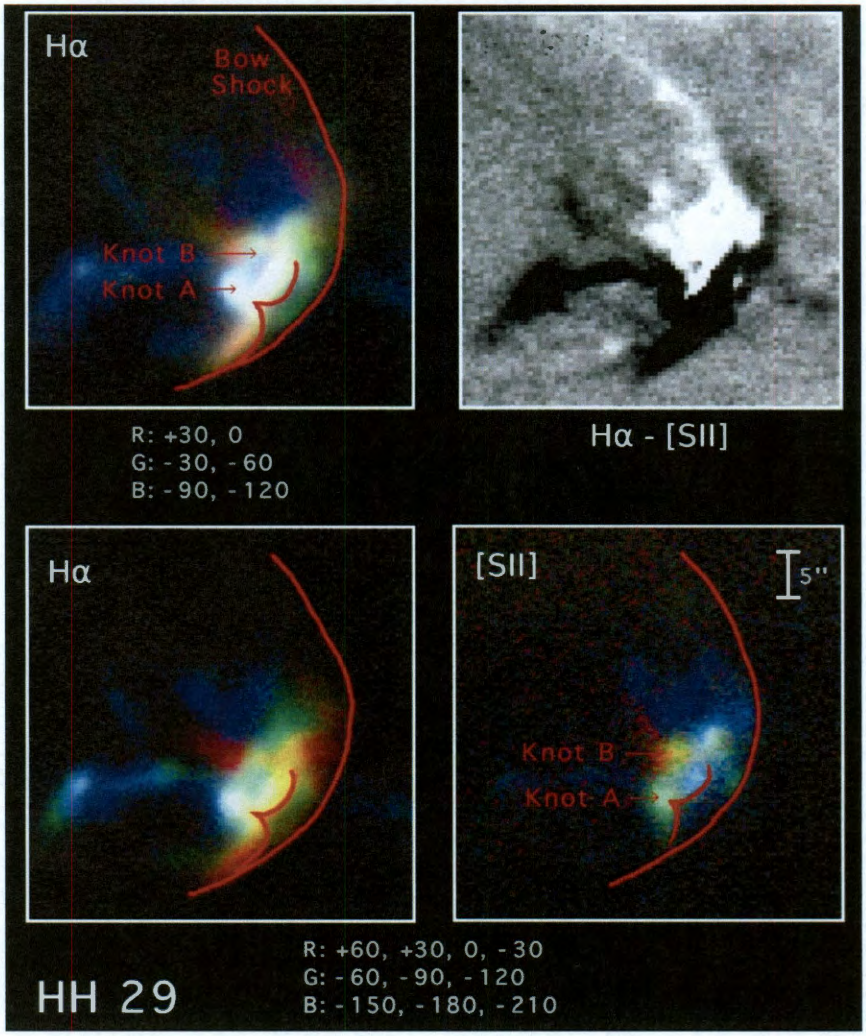

Figure 3: Radial velocity maps of Hα taken with a Fabry-Perot spectrometer. The radial velocities have been binned, with blue being rapidly toward the observer and red being (mostly) away from the observer. Velocity bins are labeled below individual images and are in km/s, with the stated value being the center of the bin. White indicates all ranges of velocities are present. This occurs at knots A and B, suggestive of material flowing around a clump. The upper right panel shows Hα minus [SII], where black is an excess of Hα and white is an excess of [SII]. Hα clearly dominates the lower half of HH29, and [SII] dominates the upper half. Image from (Hartigan et al. 2000)

1999, also looked at images of HH 29 taken seven years apart Figure 4, yielding Hα difference images showing motions within the object.

Some particular details from the above mentioned images that we want to be able to recreate in our simulations are:

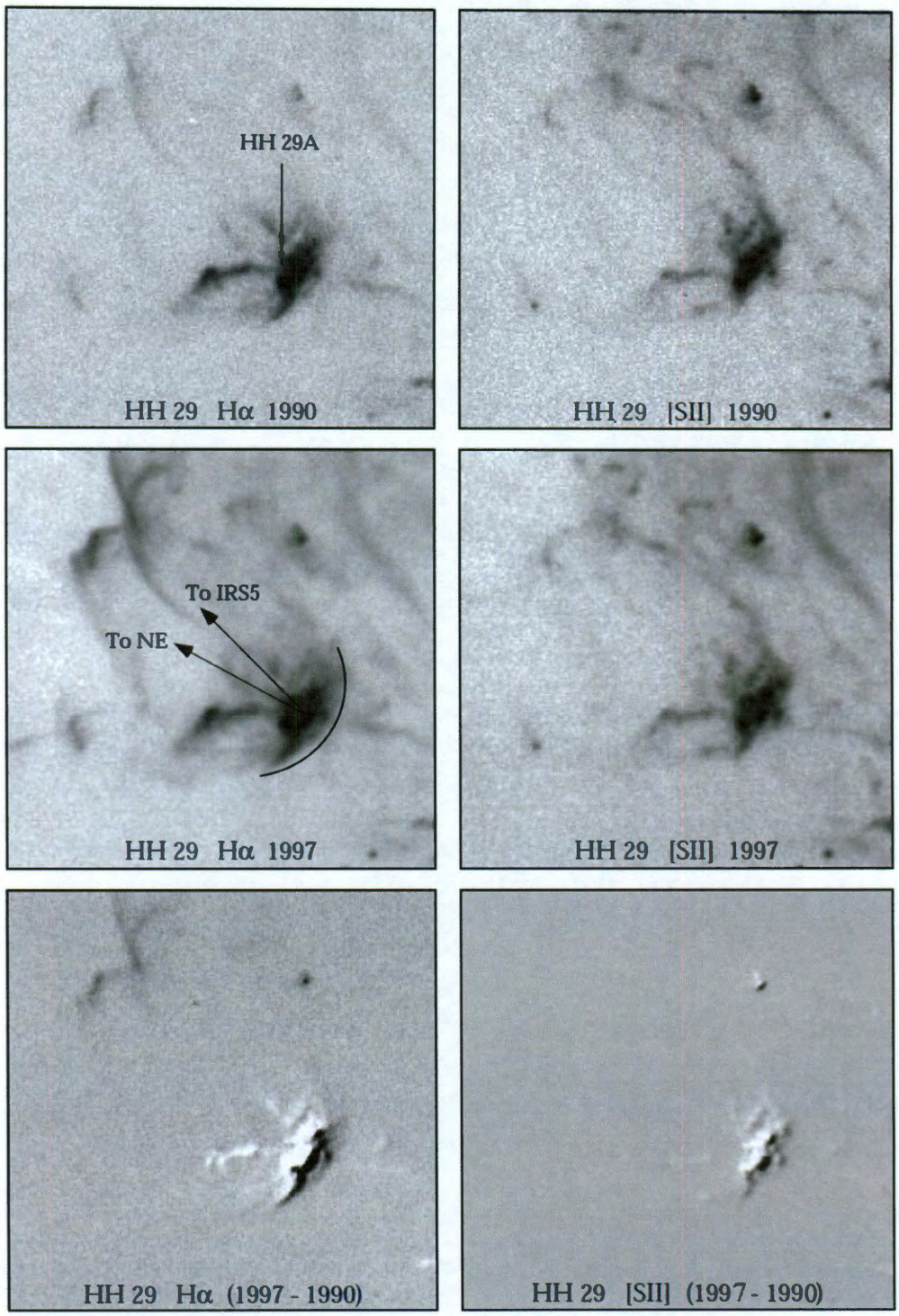

Figure 4: Hα (left) and [SII] (right) images from 1990 (top row) and 1997 (middle row). The bottom row shows a subtraction of the 1990 images from the 1997 images, where black indicates material in the 1997 image, and white indicates the material as it was in 1990. The large clumps do not appear to have moved much compared to the bow shock.

1) A bow shock with Hα along the edge, followed by [SII] emission, as seen in Figure 2 (see section 2.1 for explanation).
2) Reverse bow shocks, such as the one labeled `A' in Figure 2, which are most likely due to a clump that has been overrun by the flow.
3) Large line widths at the reverse bow shocks, suggestive of splattered material, with velocities both toward and away from us.
4) Emission line ratios and fluxes, from which we can determine information on the properties of the gas.
5) Slower proper motions of the suspected clumps within the jet.
6) The number of clumps and their positions.

(Hartigan et al. 2000) also presented an Hα minus [SII] image (see Figure 3, upper right panel) which can be used to help check the validity of the simulations. As explained below in section 2.1 we expect Hα immediately behind the shock fronts, with [SII] in the cooling zones behind it, or at the lower velocity oblique shocks from the wings of the bow.

1.4 AstroBEAR and Numerical Simulation Codes

Numerical simulations are an important tool in the study of astrophysical phenomena. In order to get a full view of just about any event, a model is needed, since astrophysical timescales are so large. Often the physical processes are not fully understood, and numerical modeling allows us to explore the physics and the parameters involved in order to better understand the processes. Most current codes have many of the same features, such as adaptive mesh refinement (AMR) which allows the code to

increase resolution only in sections of the grid where it is needed , i.e. where lots of changes to the fluid is occurring in a small area or volume. By only refining certain areas, higher resolution can be achieved with less time and memory required. Most codes are also parallelized now, permitting a single simulation to be split up among many processors, completing the simulation in a far shorter time. Some of these common codes used for modeling astrophysics are Flash (Fryxell, et al., 2000), Enzo (O'Shea, et al., 2004), Orion (Herman, et al., 2007), ZEUS (Stone and Norman, 1992), and AstroBEAR (Cunningham, et al., 2009).

AstroBEAR, from the University of Rochester, is a 3D MHD code based on BEARCLAW (Boundary Embedded Adaptive mesh Refinement Conservation LAW package) with AMR and parallelization. Two things make AstroBEAR stand out from its peers. One is that it has recently had added to it the capability to simulate laboratory experiments using a real equation of state (Carver 2010). The second important piece of AstroBEAR is that it has proper cooling and particle tracking in it, meaning that valid emission line maps can be obtained for astrophysical simulations. This is vital for comparisons with observations, since it is only through emission lines that we witness such things as HH objects.

1.5 Laboratory Experiments

Experiments in the laboratory are exploring many different areas of astrophysics including the jets and shocked clumps discussed in this thesis. Large laser facilities in the U.S. used for these experiments include the Laboratory for Laser Energetics (LLE) in Rochester, NY, the Z Machine at Sandia National Laboratory, and the new National

Ignition Facility (NIF) at Lawrence Livermore National Laboratory. Experiments at these facilities include those looking to simulate shock-clump interactions (Rosen et al. 2009) (see Chapter 5 for some discussion on this), deflected jets (Hartigan et al. 2009), magnetized jets (Lebedev, et al., 2004), and blast waves (Drake, et al., 2009), among others.

These experiments are in the high energy density regime, a far cry from the non-LTE densities of HH objects. However, the proper experimental design will allow for certain variables to scale to the astrophysical regime (Coker et al. 2007), (Ryutov et al. 1999). This means that the kinematics at least can be compared. Of course there is no emission from the experiments that we can compare with observations, so what we learn from the laboratory directly is limited, but it does give us a controlled environment in which we can explore the same dynamics we observe in astrophysical events.

Numerical modeling is also a large factor in these experiments. Codes such as the RAGE code from Los Alamos National Laboratory, or PETRA from AWE are used to help plan and simulate the laser experiments. While the experiment may only give a single snapshot in time, a numerical simulation shows the entire event. If a code can model both the high energy density laboratory and the astrophysical regimes, then there can be a self-consistent comparison of simulations, experiments, and observations.

Chapter 5 will briefly look at recent shocked clump experiments and the numerical models that accompany them, and discuss their relevance to my simulations of HH 29.

Chapter 2

Shocks and Clumps

2.1 How shocked clumps explain observations

The observed line emission of HH objects is the result of shock heated gas, so we must know how the material behaves as it passes through a shock front. Figure 5(a) shows a planar shock front, in the reference frame of the shock. In this case, the ambient medium, with temperature T_1 and density n_1, is moving into the shock front at the shock speed, v_1. The jump conditions for a shock, i.e. the post-shock conditions, are (Landau and Lifshitz 1987):

$$\frac{\rho_2}{\rho_1} = \left(\frac{v_2}{v_1}\right)^{-1} = \frac{(\gamma+1)}{(\gamma-1)+\frac{2}{M^2}} \quad , \tag{2.1}$$

$$\frac{T_2}{T_1} = \frac{2\gamma(\gamma-1)}{(\gamma+1)^2} M^2 \quad , \tag{2.2}$$

where ρ is the mass density, γ is the ratio of specific heats, c_p/c_v (also called the `adiabatic index'), T is the temperature, M is the Mach number, and equation 2.1 has made use of the conservation of momentum: $\rho_2 v_2 = \rho_1 v_1$. Note also that $\frac{\rho_2}{\rho_1} = \frac{n_2}{n_1}$. For a strong shock (Mach number, $M >> 1$) and $\gamma = 5/3$ for a monatomic gas, these give us:

- $v_2 = \frac{3}{4} v_1$ ($v_2 = \frac{1}{4} v_1$ in frame of shock) (2.3-a)

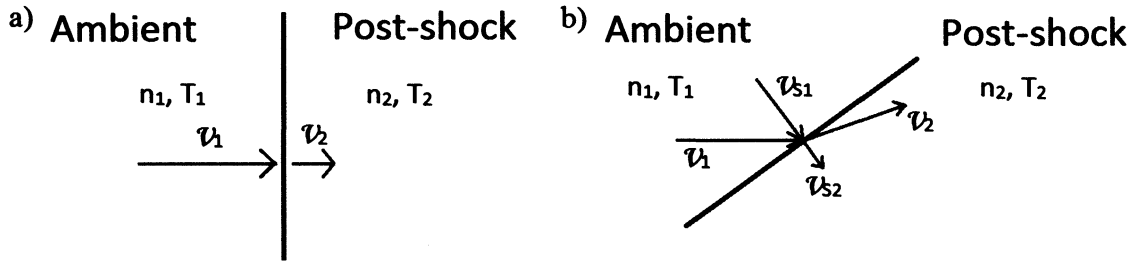

Figure 5: a) Planar shock in the shock front's frame of reference. b) Oblique planar shock in the shock front's frame of reference. Here, v_{s1} is the relevant shock velocity, and v_{s2} is the post-shock velocity, calculated from v_{s1}.

- $n_2 = 4n_1$ (2.3-b)
- $T_2 = \frac{3}{16}\frac{\mu m v_1^2}{k_B}$ (2.3-c)

The results also apply to an oblique planar shock, with the difference that the shock velocity is the velocity perpendicular to the shock front (see Figure 5(b)).

In the case where there is no cooling and the shock is in steady-state, these post-shock values will not change. The case involving cooling will be discussed in section 3, but the key detail relevant to emission is that the temperature rises drastically immediately behind the shock. For a fast enough shock, this means that Hydrogen can be collisionally excited (see section 3.2b), and we get Hα emission at the shock front. The gas then cools downstream of the shock, and we get [SII] emission and some more Hα from recombination (see section 3.2). This provides the Hα and [SII] separation that we see in HH objects.

To see how a bow shock model, in which a bow shock overruns a clump, applies to HH 29, we can look at Figure 6 to examine the different parts of a bow shock and a shocked clump. In Figure 6(a) we are in the frame of the ambient medium, labeled material 1A, so that $v_{amb} = 0$. The jet of faster material, labeled material 2J and having

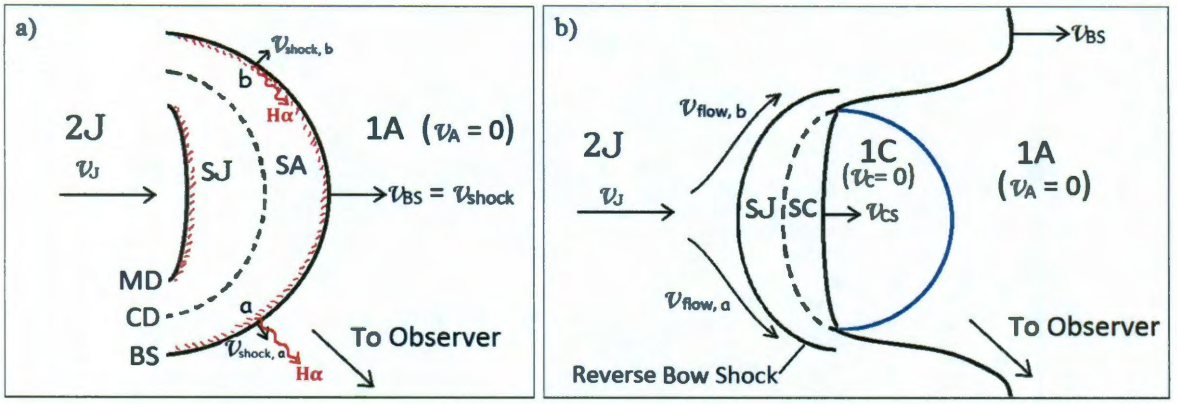

Figure 6: (a) Schematic of a bow shock, in the reference frame of the ambient material, 1A ($v_A = 0$). The jet (2J) flows from left to right with speed v_J, shocking the ambient material, forming a bow shock. As the ambient material passes through the bow, it becomes shocked ambient (SA). The bow shock moves with a speed less than v_j ($v_{BS} = ¾\ v_j$ for strong shocks). The jet shocks against SA, creating the mach disk (MD), and the jet material passing through MD is shocked (SJ), creating a contact discontinuity (dashed line, labeled CD) between SJ and SA. Note that Hα emitted immediately behind the bow shock will have different radial velocities, since the material has velocities in different directions (e.g. v_a and v_b). Also note that v_b and v_a will result in a lower shock speed than v_{BS} due to its obliqueness. (b) Schematic of a reverse bow shock and shocked clump. As the initial bow shock runs over the stationary clump it creates a shock moving into the clump with speed v_{CS}, behind which is shocked clump material (SC). The initial bow shock wraps around the clump, and the jet shocks against the SC material, forming a reverse bowshock and a shocked jet (SJ) region. Again, there is a contact discontinuity between the two shocked materials.

speed v_{jet}, is supersonic with respect to the ambient. This creates a bow shock, labeled BS, between the jet and the ambient materials. The bow shock moves at a speed v_{shock}, which is less than v_{jet}. The ambient material passing through the shock front from the right becomes shocked and is labeled SA, for shocked ambient. Because this shocked material is moving slower than the jet, the jet will actually form another shock against the back of the shocked region, referred to as the mach disk (MD) (Hartigan 1989). The jet material passing through the MD becomes shocked, and is labeled SJ. At the interface of SA and SJ is a contact discontinuity (CD), which arises due to the shocked regions not knowing about each other's shocks (e.g., information about the reverse shock has not propagated to the shocked ambient region); in reality, there is probably some mixing of the two shocked materials in that region. We therefore have two shock fronts, one forward facing, and one rear facing. If the jet is much denser than the ambient medium,

then the rear-facing shock will have a much lower shock velocity, since it is just the difference between v_{jet} and v_{MD}, which may result in a weak shock (M only slight > 1) and not produce collisionally-excited Hα. The bow shock has wings that curve in such a way that their angle eventually reaches the Mach angle, defined to be where v_{shock} (which equals $v_{\perp}$ as noted in Figure 5(b) is equal to the sound speed, and the shock disappears (Hartigan et al. 1987).

Figure 6(b) shows the shock overrunning a clump. We now have, in the front, stationary clump material (1C) passing through the shock front and becoming shocked clump material (SC). Again the jet material (2J) piles into this, resulting in a reverse shock front and shocked jet material (SJ), with a contact discontinuity (CD) between SC and SJ. Because the initial bow shock passing on either side of the clump wraps around it, we end up with the reverse shock becoming a reverse bow shock, with a gap in front of the clump on the downstream side, which is roughly the same diameter as the clump.

Also shown in Figure 6 is the velocity at various positions along the bow shock. The edges of the bow shock in 6(a) are lower velocity, oblique shocks. This can cause the post-shock temperature to be low enough that there is no Hα from collisional excitation at the shock front. We also note that an observer would see material moving both toward and away, causing emission to be both blue- and red-shifted. We should observe the largest spread of velocities at the apex of the reverse bow shock.

Returning to the observations of HH 29, we can now examine the details in terms of shocked clumps. The numbers below correspond to the observations noted in section 1.3.

1) The forward facing bow shock shows up primarily in Hα (red), with [SII] (green + blue) being emitted behind it. This tells us that there is the expected collisionally excited Hydrogen immediately behind the shock front, followed by an extended cooling zone.
2) We see apparent reverse bow shocks in HH 29, of which the possible clump labeled A in Figure 2 is the clearest example. This reverse bow shock is bright in Hα as expected, again followed by [SII].
3) The large line widths noted in Hartigan et al. 2000, combined with the radial velocities being both negative and positive (and both being bright at the locations of the presumed clumps, see Figure 3, indicate the shocked gas is being deflected around the clumps. As the gas curves around the clump, we see less spread in radial velocities as it becomes more aligned in the direction of the bulk flow of the jet.
4) Emission line fluxes will be dependent on shock velocities, both for the bow shock, and any clump/reverse bow shocks.
5) Devine et al., 1999 noted that the clumps do not move much in the seven year period between images, indicative of low velocity or stationary clumps that have been recently hit by the jet and are being accelerated.
6) The current positions of clumps will help constrain any models, as the parameter space for densities and initial positions is explored.

2.2 Analytical Expectation for Clump Acceleration

When we simulate HH 29, we would like to be able to examine clump separation as a possible parameter. In order to do so, the shocked clumps must accelerate as expected. We can determine the expected acceleration based on the conservation of momentum and balancing ram pressures. If the material sticks to the clump, then a clump that is hit and accelerated by a constant velocity jet should be accelerated to half the jet speed when the mass of jet material sticking to the clump is equal to the initial clump mass, m_0. In this case we can take as a standard time, τ, the time required for m_0 worth of jet material to stick to the clump:

$$\tau = \frac{m_0}{A\rho_0}\frac{1}{v_0} \ . \tag{2.4}$$

Here, ρ_0 is the initial density of the clump, v_0 is the initial velocity of the clump, and A is the cross-sectional area of the clump. Beginning with conservation of momentum, we have:

$$m_0 v_0 = mv \ , \tag{2.5}$$

where mv is at some future time t. We can look at this from the frame of reference of the jet, in which case the clump enters the jet with a negative velocity and slows down. Then, equating the ram pressure ($P_{ram} = \rho v^2$) with force/area, and taking the densities of the jet and clump to be equal, $\rho_{jet} = \rho_{clump} = \rho = \rho_o$, we have at time t:

$$P = \rho v^2 = \frac{F}{A} = -\frac{m}{A}\frac{dv}{dt} \ , \tag{2.6}$$

where: $F = ma = m\frac{dv}{dt}$.

Applying conservation of momentum for m gives us:

$$\rho v^2 = -\frac{m_0 v_0}{Av}\frac{dv}{dt} \tag{2.7}$$

$$-\frac{1}{v^3}dv = \frac{\rho_0 A}{m_0 v_0}dt = \frac{1}{\tau v_0^2}dt \quad . \tag{2.8}$$

Integrating v from v_0 to v, and t from 0 to t, we get:

$$v(t) = \frac{v_0}{\left(1+2\frac{t}{\tau}\right)^{1/2}}. \tag{2.9}$$

We also want to be able to compare simulations to the case in which the jet material does not stick to the clump, but rather flows around it as a laminar flow. In this case the mass of the clump remains constant with time, so $m = m_0$. For laminar flow around an obstacle, the pressure at the stagnation point is (Landau and Lifshitz 1987):

$$P = \frac{1}{2}\rho v^2 = \frac{F}{A} \sim -\frac{m_0}{A}\frac{dv}{dt}, \tag{2.10}$$

where the '~' allows for some geometrical factor of order unity specific to the shape of the object. Rearranging we get:

$$\frac{1}{2}\frac{\rho A}{m_0}dt \sim -\frac{1}{v^2}dv \quad . \tag{2.11}$$

Integrating as before and substituting in τ now gives us:

$$v(t) \sim \frac{v_0}{1+\frac{t}{2\tau}} \quad . \tag{2.12}$$

We will use these equations in section 4.1 to compare with simulations of a clump accelerating in a jet.

Chapter 3
Cooling and Line Emission

3.1 – Cooling and Line Emission: Necessity & Implementation

The structure of a shock is highly influenced by the cooling processes in the post-shock gas. As HH objects cool radiatively, they lose the post-shock pressure support of a non-cooling gas, which causes the width of the shocked area to collapse. In the event of a shocked clump, the shock front will wrap around the clump far more tightly than in an adiabatic case (Yirak et al. 2010). It is also due to the cooling that we are able to observe HH objects, as it is the line emission from the cooling processes that we detect. Therefore, any attempt to model observations of an HH object must include proper cooling and line emission.

Observationally, line emission also provides important information about the gas. Because HH objects are optically thin, we see everything that is emitted, which means we see the entire object, projected onto the plane of the sky. Beyond the dynamics discussed above (shock velocities from the lines involved, radial velocities from the line widths, etc.), the ratios of certain lines can tell us about the electron densities, temperatures, etc.

AstroBEAR includes cooling from two main areas of contribution. The original cooling in AstroBEAR came from the cooling curve of Dalgarno & McKay (Dalgarno and McCray 1972), which includes Hydrogen and Helium collisional excitation, plus cooling due to collisional excitation of metals (`metals' here refers to trace elements,

which is any element higher than He). This has been modified as described below in section 3.2c to remove H excitation to allow that process to be included in the second cooling routine. This second contribution is cooling due to the collisional ionization of HI, HeI, and HeII, followed by recombination of HII and HeII, as well as collisional excitation of H. In order to do this, AstroBEAR tracks the particle densities of these atoms, as well as n_e, the electron density. This allows it to calculate Hα emission from collisional excitation and recombination (section 3.3a), as well as line emission from OI, OII, NI, NII, and SII due to collisional excitation (see section 3.3b).

3.2 – Cooling Processes

An object that radiatively cools loses energy when its thermal energy is removed from the system, radiating line emission in the process. The energy loss comes when an electron recombines (removing its contribution to the thermal energy of the gas), or collides with an atom, exciting it, and thus departing with decreased energy. In AstroBEAR, the processes explicitly included are (1) collisional ionization followed by recombination (section 3.2a), and (2) collisional excitation of Hydrogen (section 3.2b). In process (1), a free electron ionizes HI, HeI, or HeII. If that electron recombines, then it loses thermal energy in the amount of the ionization energy, plus whatever excess kinetic energy it had. In (2), the free electron loses kinetic energy in the amount of the excitation energy imparted to the H atom. AstroBEAR tracks the number of these interactions (by tracking n_e and the number of H and He in different ionization states), allowing it to calculate the total cooling from recombination and collisional excitation.

AstroBEAR also includes cooling due to collisional excitation of metals based on the Dalgarno-McCray cooling curve (see section 3.2c).

3.2(a) – Collisional Ionization and Recombination of Hydrogen

When an electron collides with and ionizes an atom, no energy is lost from the system; this loss does not actually occur until recombination, when the energy is radiated away. However, some of its kinetic energy goes to overcoming the binding energy of the bound electron. This reduces the thermal energy within the system, which in turn reduces the pressure. Because pressure affects the fluid flow in AstroBEAR, we remove the energy at this point to reflect the change in pressure (Carver 2010).

To calculate the collisional ionization energy loss, we need ionization coefficients and rates for H. For the collisional ionization rate coefficients, α_{ci}, we have (Mazzotta et al. 1998):

$$\alpha_{ci} = 6.69 \times 10^{7} \frac{e^{-x}}{(kT)^{\frac{3}{2}}} F(x) \quad (\mathrm{cm}^3/\mathrm{s}), \tag{3.1}$$

where

$$F(x) = A[1 - xf_1(x)] + B[1 + x + x(2 + x)f_1]Cf_1(x) + Dxf_2(x) \tag{3.2}$$

and

$$x = \frac{I}{kT} \tag{3.3}$$

Here I is the ionization energy, f_1 and f_2 are integrals over time, and the parameters A, B, C, and D can be found in Mazzotta et al. and references therein. The cooling rate, Λ_{ci},

then comes from the number of colliders (electrons and species X, which here includes H, HeI, or HeII), collision rate, and energy lost per collision:

$$\Lambda_{ci} = I_x n_e n_X \alpha_{ci} \qquad (erg\ cm^{-3}\ s^{-1}), \tag{3.4}$$

where I_X is the ionization energy of species X, n_e is the number density of electrons, and n_X is the number density of species X.

When the electron recombines, we assume it will cascade down to ground state and radiate away the equivalent of its ionization energy (which we took into account with Λ_{ci}). However, these electrons have, on average, kinetic energy greater than I_X, by an amount on the order of $k_B T$ (Osterbrock and Ferland 2006), which we take as the energy lost per recombination. We consider only radiative recombination here, and again we need the rate and rate coefficient. We get the radiative recombination rate coefficient, $\alpha_{r,rad}$ from (Verner and Ferland 1996) (VF96):

$$\alpha_{r,rad} = a\left[\sqrt{\frac{T}{T_0}}\left(1+\sqrt{\frac{T}{T_0}}\right)^{1-b}\left(1+\sqrt{\frac{T}{T_1}}\right)^{1+b}\right]^{-1} \quad (\mathrm{cm^3/s}). \tag{3.5}$$

Parameters a, T_0, T_1, and b can be found in VF96 for HI, HeI, and HeII, and are valid for temperatures from 3 K to 10^9 K. Therefore, the rate of energy lost due to radiative recombination, Λ_{rec}, is:

$$\Lambda_{rec} = k_B T n_e n_X \alpha_{rec} \qquad (erg \cdot cm^{-3} \cdot s^{-1}), \tag{3.6}$$

where now X refers to HII, HeII, or HeIII.

3.2(b) – Collisional Excitation of Hydrogen

We have added cooling due to excitation of ground state Hydrogen to electronic energy levels 2 through 5 and its subsequent decay back to ground. As with ionization and recombination, this requires the collisional excitation rate coefficients and rates. These we took from (Anderson et al. 2000) and (Anderson et al. 2002), where the coefficient for excitation from level i to j, q_{ij}, is given as:

$$q_{ij} = \frac{2\sqrt{\pi}\alpha c a_0^2}{\omega_i}\sqrt{\frac{I_H}{k_B T_e}}\,exp\left(-\frac{\Delta E_{ij}}{k_B T_e}\right)\Upsilon_{ij} \qquad (\mathrm{cm^3/s}). \qquad (3.7)$$

Here, $2\sqrt{\pi}\alpha c a_0^2 = 2.1716 \times 10^{-8}$ cm^3/s, ω_i is the statistical weight of H in level i ($\omega_i = 2$ for $i = 1$), $I_H = 13.6$ eV is the ionization energy of H, and ΔE_{ij} is the required energy to transition from level i to level j. The effective collision strengths, $\Upsilon_{ij}(T)$, are tabulated for transitions not just between levels n, but between all nℓ, where each i and j represent a given nℓ, and n is from 1 to 5, ℓ is from 0 to 4 (ie. s, p, d, f, g). For example, $i,j = 1,12$ represents the transition from n = 1, $\ell = 0$ to n = 5, $\ell = 2$. We assume all excitations are from ground state and only accept transitions up to j = 15 (n = 5, $\ell = 4$). Here we assume that H is all in the ground state, so that $i = 1$ for all transitions; the total collisional excitation energy rate loss coefficient, for all transitions, is then given by:

$$\alpha_{ex} = \sum_{j=2}^{15} \Delta E_{1j} q_{1j} \qquad (\mathrm{erg \cdot cm^3 \cdot s^{-1}}). \qquad (3.8)$$

This gives us an energy loss rate by collisional excitation of H:

$$\Lambda_{H,ex} = n_e n_{HI} \alpha_{ex} \qquad (\mathrm{erg \cdot cm^{-3} \cdot s^{-1}}). \qquad (3.9)$$

Electron densities are not expected to reach 10^4 cm^{-3}, putting us in the low density limit and allowing us to disregard collisional de-excitation.

3.2(c) – Cooling when T > 10^4 K: A Modified Dalgarno-McCray Cooling Curve

As mentioned above, the Dalgarno-McCray (DM) cooling curve, shown in Figure 7, includes collisional excitation of H, He, and metals in its formation. However, this curve assumes ionization equilibrium, in which the rate of collisional ionizations equals the rate of recombinations, such that the ionization fraction is constant for a given temperature. This is not at all the case in a post-shock region. The post-shock temperature rises so quickly that it takes some time for the H to ionize, by which time the temperature has cooled. This means that for a given temperature, the DM curve assumes a higher number of ionized H, which in turn means there are more free electrons available for collisions, which leads to a higher cooling rate than is actually the case in the post-shock region.

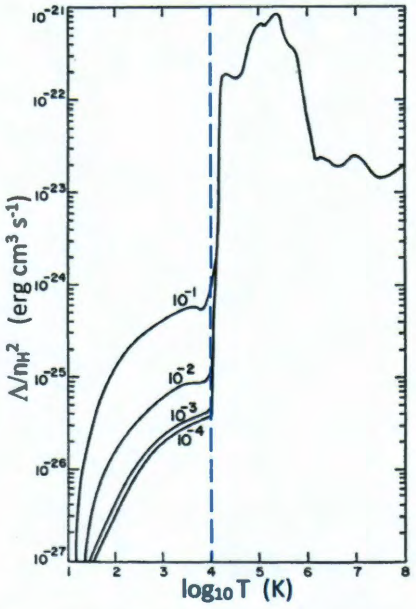

Figure 7: The Dalgarno-McCray cooling curve. Low temperature cooling comes from collisional excitation of the fine structure levels of metals. Higher temperature cooling comes from excitation of electronic energy levels of metals (yields forbidden line emission). We do not use this curve below T = 10^4K (marked by dashed line) due to the dependence on ionization fractions of the different metals, where the numbers on the curves indicate the total fractional ionization $x = n_e/n_H$.

AstroBEAR does not explicitly calculate cooling from metals when $T > 10^4$ K, so this curve is still needed for that purpose, but we already have collisional excitation of H as described above. That means that we have to subtract off the equilibrium H excitation cooling from it. To do this, we look at how the DM curve is implemented. In Figure 7, the curve plots the cooling Λ in erg·cm^3·s^{-1}, which is actually a cooling rate divided by number density squared, or Λ/n_H^2, where n_H is the total Hydrogen number density. Therefore, when defining our H equilibrium cooling, we have to make sure we divide it as well before subtracting it from the DM curve. We obtained the H equilibrium curve from the Anderson data in the same way as section 3.2(b), after first determining the equilibrium ionization fraction of H for each temperature by balancing collisional ionization and recombination:

$$n_e n_{HI} \alpha_{ci} = n_e n_{HII} \alpha_r \tag{3.10}$$

$$\frac{n_{HI}}{n_{HII}} = \frac{\alpha_r}{\alpha_{ci}} \quad . \tag{3.11}$$

This gives

$$\frac{n_{HII,eq}}{n_H} = X_{H,eq} = \frac{n_{HII,eq}}{n_{HI,eq}+n_{HII,eq}} \quad , \tag{3.12}$$

$$X_{H,eq} = \left(1 + \frac{\alpha_r}{\alpha_{ci}}\right)^{-1} \tag{3.13}$$

where $X_{H,eq}$ is the ionization fraction of Hydrogen in equilibrium, and α_r and α_{ci} are the radiative recombination and collisional ionization rate coefficients of section 3.2a, and are dependent on temperature. When defining our H-equilibrium cooling rate, $\Lambda_{H,eq}$, we can then use:

$$\frac{\Lambda_{H,eq}}{n_H^2} = \frac{n_{e,eq}}{n_H}\frac{n_{HI,eq}}{n_H}\alpha_{ex} \tag{3.14}$$

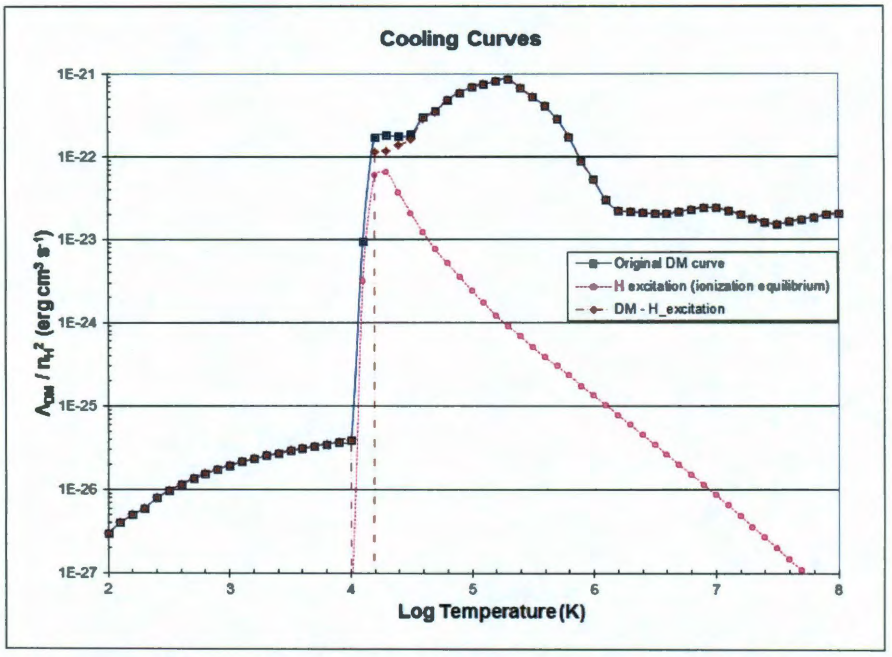

Figure 8: The original Dalgarno-McCray cooling curve (solid line with square markers), overplotted with the curve for equilibrium H excitation cooling (dotted line with circles) and the subtraction of the two curves (dashed line with diamonds).

$$\Lambda_{H,eq} = n_H^2 X_{H,eq}(1 - X_{H.eq})\alpha_{ex} \ , \qquad (3.15)$$

Where we have assumed that $n_{HII,eq} = n_{e,eq}$. By subtracting the above from the DM cooling curve we get a curve that is just metal cooling, shown in Figure 8. However, this curve still assumes ionization equilibrium. Because the electrons effectively all come from ionized H, this means that the subtracted curve is still over-cooling. To help reduce this, we multiply by $n_e/n_{e,eq} = X_H/X_{H,eq}$, such that our final metal cooling rate, at $T > 10^4$ K, is calculated as:

$$\Lambda_{metal,high\,T} = n_H^2 \left(\frac{\Lambda_{DM}}{n_H^2} - \frac{\Lambda_{H,eq}}{n_H^2}\right)\left(\frac{X_H}{X_{H,eq}}\right) \ . \qquad (3.16)$$

At temperatures less than 10^4 K the DM cooling curve is highly dependent on the ionization fractions of the metals, which affect the total fractional ionization. Figure 7 shows how the curve differs for different assumptions of fractional ionization. For these

reasons the DM curve is not used at $T < 10^4$ K, and the total cooling rate calculated in AstroBEAR at the time these simulations were run is the sum of all the above cooling mechanisms:

$$\Lambda_{total} = \Lambda_{ci} + \Lambda_{rec} + \Lambda_{H,ex} + \Lambda_{metal,high\,T} \qquad (\text{erg}\cdot\text{cm}^{-3}\cdot\text{s}^{-1}) \quad (3.17)$$

3.2(d) – Cooling when $T < 10^4$ K: Low Ionization Forbidden Lines

The simulations presented below in chapter 4 do not include any cooling at temperatures below 10^4 K due to the fact that AstroBEAR did not have proper cooling implemented for that range when the simulations were run. It has since had cooling added for $T < 10^4$ K which will be used for future simulations. As mentioned above in section 3.2(c), the DM cooling below 10^4 K made assumptions about the total ionization fraction of metals, including the assumption of ionization equilibrium. To properly deal with this cooling, however, we require accurate forbidden line lists and ionizations fractions that are not in equilibrium.

In order to accomplish this we consider only the seven most abundant elements after Hydrogen and Helium: Carbon, Nitrogen, Oxygen, Iron, Sulfur, Silicon, and Magnesium, and assume solar abundances. Since CI lines are weak, and C is easily photoionized, we take C to be all CII. The ionization states of N and O are tied to that of H through charge exchange. Their ionization fractions, X_N and X_O, depend on the ionization fraction of H, X_H, through $X_N = f(T)X_H$ and $X_O = g(T)X_H$, where f(T) and g(T) are both known functions of temperature which are described in detail in section 3.3(b). As with C, we assume all Fe, S, Si, and Mg are singly ionized since their neutral lines are

weak and they are easily photoionized. We do not need to include the doubly ionized species of these elements since the temperature is less than 10^4 K. With these number densities we are able to make a table of cooling rates as a function of X_H, T, and the electron number density, n_e. This table has been added to the AstroBEAR cooling routine, and future simulations will include it in the total cooling rate calculation as $\Lambda_{metal, low\ T}$, such that

$$\Lambda_{total} = \Lambda_{ci} + \Lambda_{rec} + \Lambda_{H,ex} + \Lambda_{metal,high\ T} + \Lambda_{metal,low\ T} \quad (\text{erg}\cdot\text{cm}^{-3}\cdot\text{s}^{-1}). \quad (3.18)$$

3.3 – Emission

Emission from a simulation is calculated in post-processing routines (a separate program after the simulation is complete), taking temperature, T, ionization fraction, X_H, electron number density, n_e, and total H number density, n_H, as inputs. The emission, in erg cm^{-3} s^{-1} str^{-1}, is then calculated as described below for Hα (section 3.3a) and the forbidden lines of [SII], [OI], [OII], [NI], and [NII] (section 3.3b). Intensity images (in erg cm^{-2} s^{-1} str^{-1}) are created by summing the emissions along the line of sight.

3.3(a) - Hα emission

In calculating Hα emission, we included Hα from recombination and from collisional excitation followed by decay. This is very similar to how we determine the cooling due to these two processes, with a few adjustments. In particular we have to tweak how we treat collisional excitation. One assumption that we make is that all electrons come from ionized Hydrogen, such that ne = n_{HII}. For recombination, we also

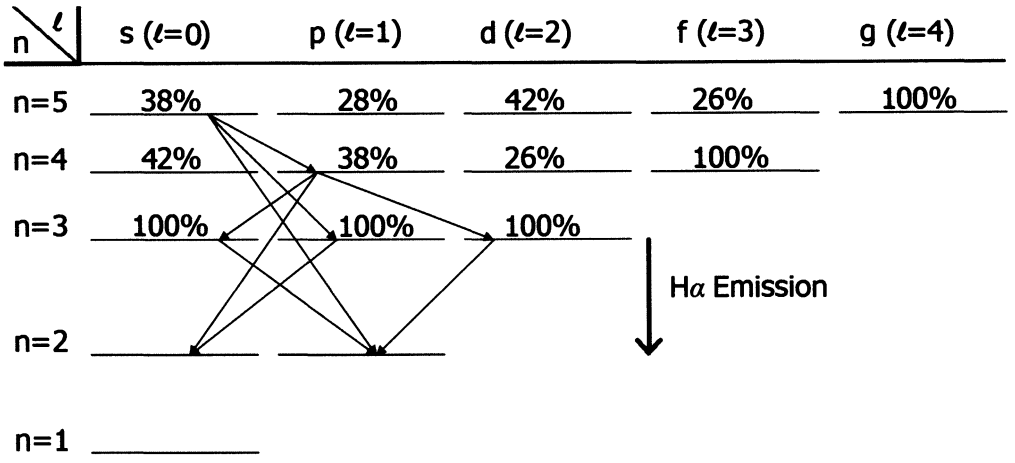

Figure 9: Probability of each possible nℓ state of excited H to emit Hα when it decays. Note that all n=3 states yield Hα 100% of the time. Transitions such as nℓ=5s to n'ℓ'=2p, however, do not produce Hα, reducing the probability that Hα will be emitted from most n=4 and n=5 initial states.

assume that all recombinations produce Hα emission. Thus the emission rate in Hα is the same as the cooling rate, divided by 4π to get it per steradian (erg·cm^{-3}·s^{-1}·str^{-1}):

$$\text{Emission}_{H\alpha,rec} = \frac{\Lambda_{rec}}{4\pi} = \frac{n_e n_{HII} \alpha_r}{4\pi} = \frac{n_{HII}^2 \alpha_r}{4\pi} \quad . \tag{3.19}$$

For collisional excitation we now consider only excitations to level n = 3,4,5. This comes from the fact that HH objects are optically thick to Lyman-α, and any excitation to level n = 2 will result in an emitted photon that does not escape from the system but is quickly reabsorbed, potentially at a higher energy level. Because these excitations also go to the different ℓ states, not all of the subsequent decay paths will yield Hα emission, and those that do will not do so at the same rate, since the spontaneous decay rate (Einstein A value) is different for each nℓ -> n'ℓ' transition. To take this into account, we calculated the branching ratios which give us the probability that a given nℓ state's decay will produce Hα, as shown in Figure 9. Hα emission due to collisional excitation is then given by:

$$\text{Emission}_{H\alpha,ex} = \frac{n_e n_{HI} \alpha_r}{4\pi} = \frac{n_{HII} n_{HI} \alpha_r}{4\pi} \quad . \tag{3.20}$$

Here α_r uses a modified version of (3.7), now given by:

$$q_{ij} = \frac{2\sqrt{\pi}\alpha c a_0^2}{\omega_i} \sqrt{\frac{I_H}{k_B T_e}} exp\left(-\frac{\Delta E_{ij}}{k_B T_e}\right) \Upsilon_{ij} P_{ij} \qquad (\text{cm}^3/\text{s}), \tag{3.21}$$

where P_{ij} is the probability of an Hα transition. Since $n \geq 3$, we now have $j \geq 4$ ($n = 3$, $\ell = 0$), which gives us:

$$\alpha_r = \sum_{j=4}^{15} \Delta E_{1j} q_{1j} \qquad (\text{erg}\cdot\text{cm}^3\cdot\text{s}^{-1}). \tag{3.22}$$

The total Hα emission is just the sum of (3.18) and (3.19):

$$\text{Emission}_{H\alpha} = \text{Emission}_{H\alpha,rec} + \text{Emission}_{H\alpha,ex} \tag{3.23}$$

3.3(b) – Emission from [SII], [OI], [OII], [NI], [NII]

Some of the most common line emission we get from HH objects comes from the forbidden lines of collisionally excited SII, OI, OII, NI, and NII. The ratios of certain lines can provide observers with details about the emitting gas. For example, [SII] λ6716/ λ6730 gives us an estimation of n_e.

Here we refer to the emissivity, j_{if}, which is the emission for a given species' transition from level i to level f, where transitions between levels $n = 1$ to 5 are considered.

$$j_{if} = \frac{n_{i,Sp} A_{if} (h\nu)_{if}}{4\pi} \qquad (\text{erg}\cdot\text{cm}^3\cdot\text{s}^{-1}). \tag{3.24}$$

where $n_{i,Sp}$ is the number density of a given species in level i, A_{if} is the Einstein A value for the decay from level i to level f, and $(h\nu)_{if}$ is the energy of that transition. The latter

two values are tabulated, but the number density must be calculated from the input values of T, n_e, X_H, and n_H.

To get $n_{i,Sp}$ we can multiply n_{Sp} by the level population $P_{i,sp} = n_{i,Sp} / n_{Sp}$. The level populations come from knowing that the system (which is non-LTE) is in statistical equilibrium, meaning we can balance the collisional excitation, de-excitation, and decay rates in and out of a given level i:

$$\sum_{\substack{i>j\ (excite\ in) \\ i<j\ (de-excite\ in)}} P_{i,Sp} n_e \alpha_{ij} + \sum_{(decay\ in)}^{i<j} P_{i,Sp} A_{ij}$$

$$= \sum_{\substack{i<j\ (excite\ out) \\ i>j\ (de-excite\ out)}} P_{i,Sp} n_e \alpha_{ji} + \sum_{(decay\ out)}^{i>j} P_{i,Sp} A_{ji} \,. \qquad (3.25)$$

This gives us $P_{i,Sp}$, but we still need n_{Sp}, which we determine from charge exchange, which couples the ionization fraction of O and N to that of H.

In charge exchange, a positive ion, e.g. O^+, meets a neutral H, forming OH^+ temporarily, before splitting. When the OH^+ splits, it can either go back to O^+ and H, or it can go to O and H^+. Therefore, charge exchange works best when the ionization energy of the two atoms is similar. This is very much the case for O, whose ionization energy is 13.62 eV, versus the 13.60 eV for H. It is less so for N (14.53 eV), but still acceptable (Hartigan and Morse 2007). Charge exchange gives us (for SpI representing OI or NI, and SpII representing OII or NII):

$$\frac{n_{SpII}}{n_{SpI}} = \frac{g_{HI} g_{SpII}}{g_{HII} g_{SpI}} \frac{n_{HII}}{n_{HI}} e^{\frac{-(\chi_{Sp} - \chi_H)}{k_B T}} \,, \qquad (3.26)$$

where the g values are the statistical weights and the χ's are the ionization energies. Combining (3.25) with assumed solar abundances, $n_{Sp,tot}$, lets us calculate n_{SpI} or n_{SpII} from:

$$n_{SpI} = n_{Sp,tot}\left(1 + \frac{n_{SpII}}{n_{SpI}}\right)^{-1}, \tag{3.27-a}$$

$$n_{SpII} = n_{Sp,tot}\left(1 + \frac{n_{SpI}}{n_{SpII}}\right)^{-1}. \tag{3.27-b}$$

We finally get $n_{i,Sp} = P_{i,Sp}n_{Sp}$, and thereby our emissivity, j_{if}. Note that we assume all S is SII, since the ionization energy of S is sufficiently low (10.4 eV) that in an HH object it is safe to assume it has all been singly ionized. We also only allow singly ionized species, since in general the temperatures involved are not enough to doubly ionize the atoms.

Chapter 4

Simulations

4.1 - Clump Acceleration: Comparison with Analytical Calculations

The analytical expectations for the timescale for a clump's acceleration by a jet were derived in section 2.2. Here we compare them to simulations of accelerated clumps in AstroBEAR. The basic set-up takes the computational grid to be filled with jet material of density $n_{jet} = 1000$ cm^{-3}, temperature $T_{jet} = 1000$ K, and speed $v_{jet} = 100$ km/s. A clump is then place into this grid with density $n_{clump} = 1000$ cm^{-3}, temperature $T_{clump} = 10$ K, and speed $v_{clump} = 0$ km/s. One grid unit length equals 2500 AU, so the entire length of this grid is 64000 AU. The clump radius, $R_{clump} = 500$ AU. These runs were done in 2.5D (cylindrical symmetry) instead of 3D, since the grid length required for acceleration made high resolution simulations prohibitive.

As can be seen in Figure 10, the clump is initially compressed in front, while also being smeared out from the back. In order to determine a speed for the clump, we took a density weighted velocity for a total area inclusive of anywhere the clump density was greater than 20 cm^{-3}. The results are shown in Figure 11. Also shown in Figure 11 are the two analytical results of section 2.2, plus an added laminar case in which R_{clump} was twice as large, and various simulations, including one with R_{clump} being twice as large, one with ρ_{clump} twice as large, and one with no cooling.

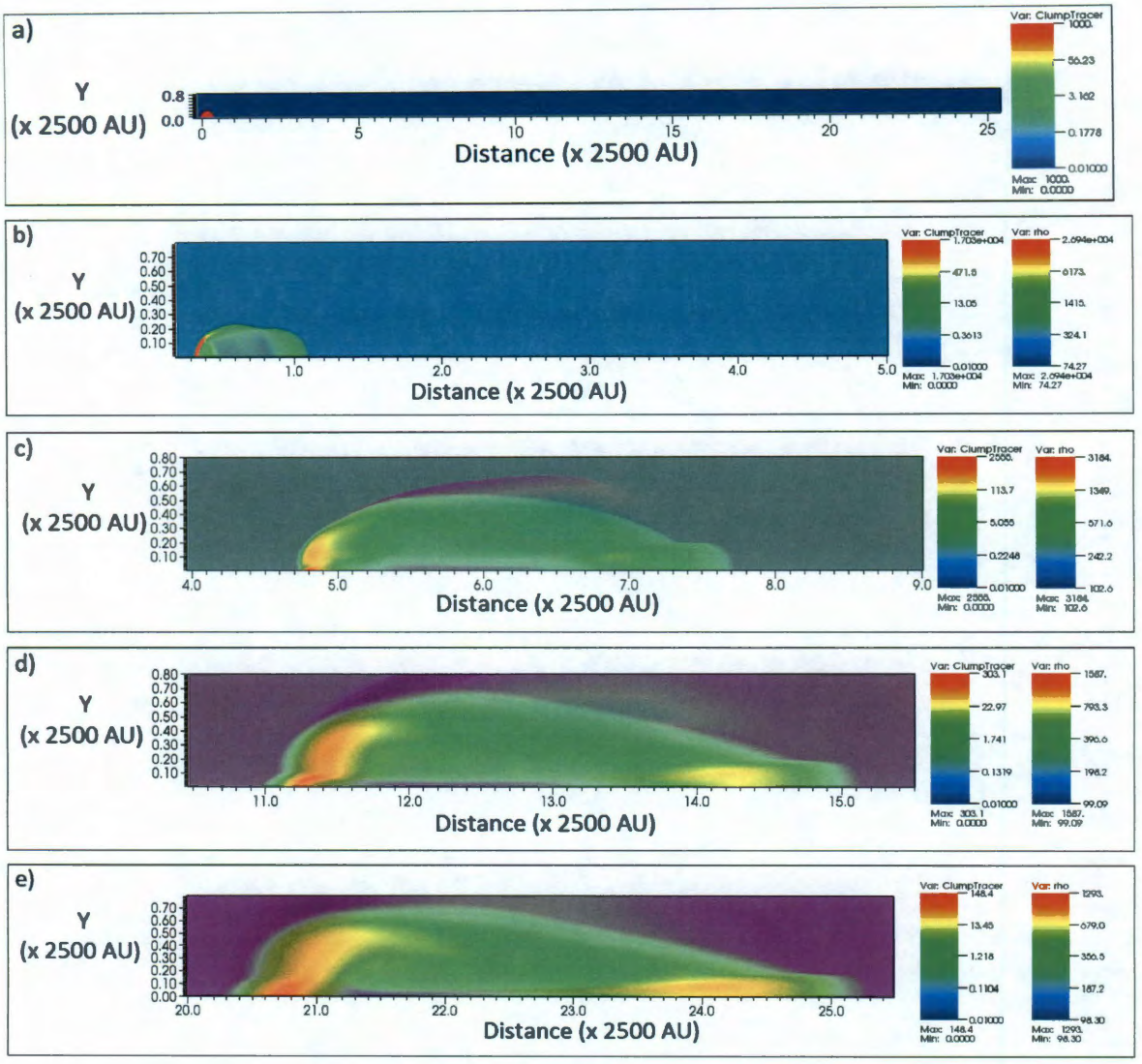

Figure 10: Clump acceleration. Images show clump density and total density at times: a) 0 yrs, b) 52.2 yrs, c) 783 yrs, d) 1630 yrs, and e) 2804 yrs. The full extent of the grid is shown in (a), whereas (b) – (e) show approximately 5 grid units (12500 AU) surrounding the extended clump.

As we can see in Figure 11, the analytic case with the jet material sticking to the clump accelerates the quickest initially, since all of the jet material that hits within the clump's cross-section helps to accelerate the clump. However, the total mass to be accelerated is increasing as well, and within about 70 years both the analytic `Laminar' and the simulated `No Cooling' cases have accelerated their clumps to higher speeds than the analytic `Material Sticks' case. The `No Cooling' case goes on to reach maximum

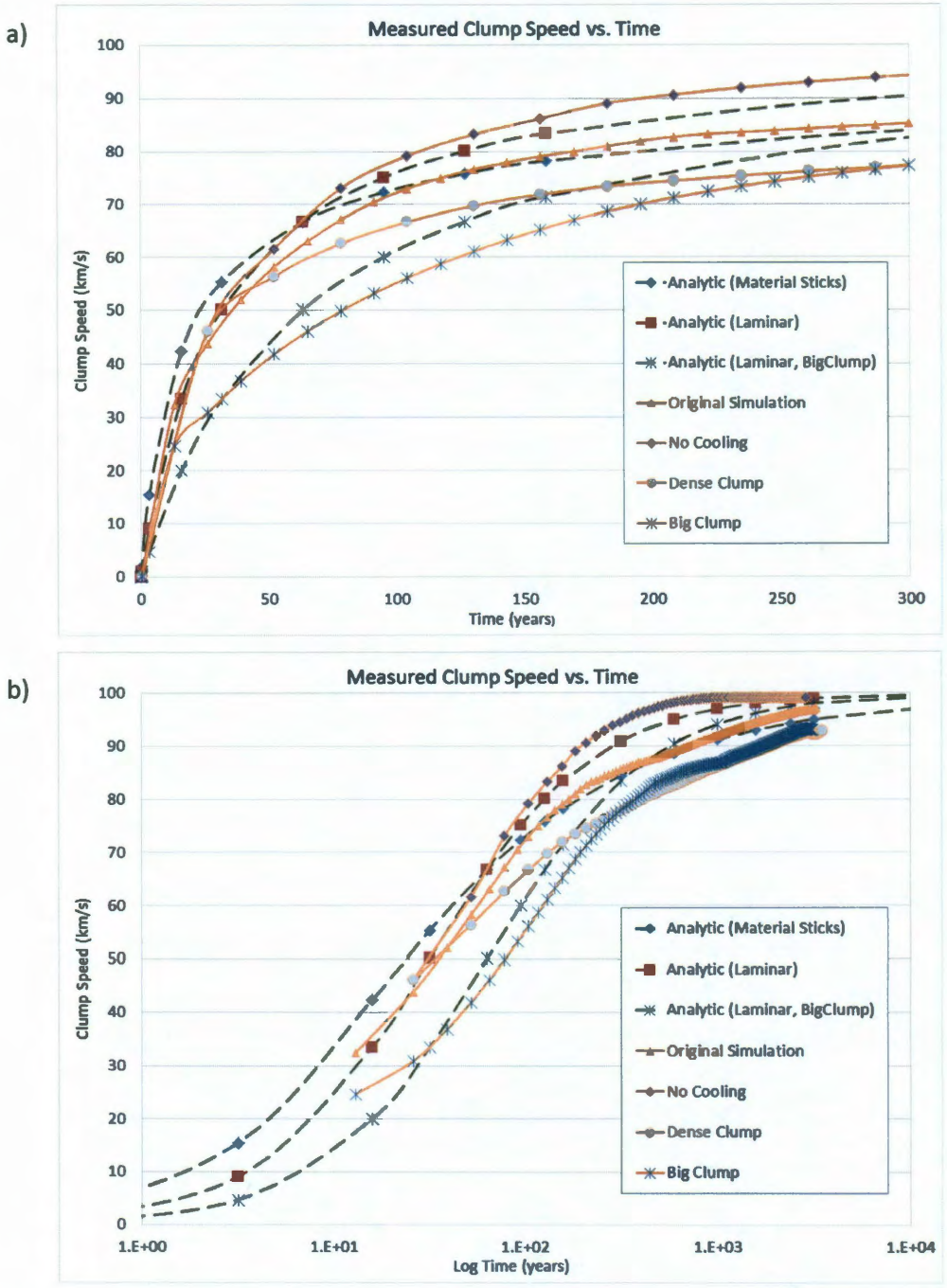

Figure 11: Plots of clump acceleration over time. a) The first 300 years, with a linear Time scale. b) The first 10,000 years, with a logarithmic Time scale. The analytic data come from the methods discussed in section 2.2. The best match here is for the simulation with no cooling (diamonds). The standard simulation with cooling (triangles, labeled 'Original Simulation') takes longer than without cooling, indicating that some of the kinetic energy is being lost as the clump cools.

clump speed the earliest of all cases. The basic cooling simulation takes much longer to accelerate, and actually ran off the grid before full acceleration occurred, though it does

reach 90% speed by ~1000 years. This slow speed up suggests that some of the kinetic energy of the jet gets radiated away in the post-shock cooling zone. The 'No Cooling' run does not suffer from this effect. It accelerates the clump at approximately the same rate as the analytic 'Laminar' case, but does not taper off as soon as that case. This may be due to the fact that the clump is more spread out, and hence more of the jet material is involved in the acceleration, so the force is increased. The other simulations show that the acceleration time is increased both by an increased size (with more mass that must be accelerated), and by an increased density, as the case should be.

The main point that we wished to establish with this exercise was that the acceleration occurs on timescales that agree with analytic expectations. While we cannot analytically calculate the acceleration with cooling, the fact that the 'No Cooling' simulation agrees well with predictions, and that discrepancies can be accounted for, add weight to the validity of the way AstroBEAR deals with these situations.

4.2 - Bow Shock Components

To simulate a bow shock, we created a jet with a velocity gradient, from v_{jet} at its center, to 0.8 v_{jet} at its edge. As the jet moves into the ambient material, it creates a shock, which is planar initially, but due to the velocity gradient it begins to take on a curved shape, and slowly develops extended wings. For these simulations, the jet conditions were: T_{jet} = 1000 K, v_{jet} = 100 km/s (Mach number = 27), n_{jet} = 1000 cm^{-3}, and a Hydrogen ionization fraction X_H = 0.01; the ambient conditions were: T_{amb} = 1000 K, v_{amb} = 0 km/s, n_{amb} = 100 cm^{-3}, and X_H = 0.01. This set-up created a shock with speed

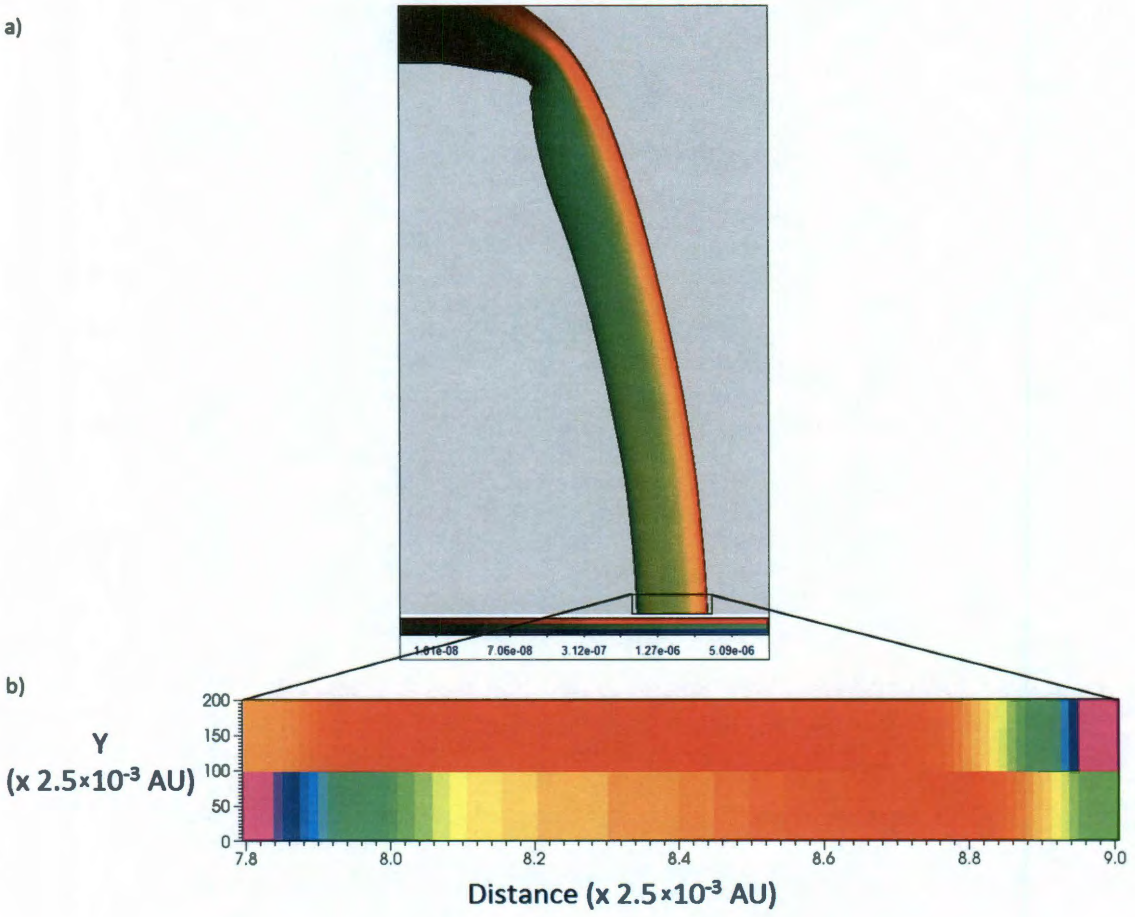

Figure 12: (a) Bow shock, shown in Hα (red) and [SII] (green). (b) Zoomed in on bottom part of bow shock, displaying the densities of the jet material on top and the ambient material on bottom.

$v_{shock} \approx 80$ km/s. We ran this simulation in 2.5-D to allow increased resolution (128 x128 cells + 3 levels of AMR; 31.25 AU grid length).

The components of a bow shock were described in section 2.1 and drawn in Figure 6. These include the ambient material (1A), bow shock front (BS), shocked ambient material (SA), contact discontinuity (CD), shocked jet material (SJ), Mach disk (MD), and jet material (2J). A simulation of a bow shock is shown in Figure 12(a) with these items labeled. All components are easily visible with the exception of the contact discontinuity. As noted in section 2.1, there is expected to be some mixing of the

shocked materials, but as Figure 12(b) shows, the peak density of the two shocked materials is offset, with SA toward the BS, and SJ toward the MD.

4.3 - Cooling Tests

AstroBEAR's cooling routines were tested two years ago against a 1-D shock code that included all the relevant atomic microphysics involved in cooling processes (Carver 2010)). The AstroBEAR simulations were accomplished by running the ambient material against a reflection boundary so that it created a planar shock. The ambient material continued to flow into this shock that puffed out until it was a steady-state planar shock with cooling zones behind it, allowing us to determine the post-shock values. The ambient material had temperature $T_{amb} = 10^4$ K, $n_{amb} = 100$ cm^{-3}, and an initial $X_H = 0.01$. We tested velocities of 40 km/s, 60 km/s, and 80 km/s at two different resolutions: 2.92 x 10^{12} cm/cell and 7.30 x 10^{11} cm/cell. The 1D shock code we used for comparison was created by John Raymond (Raymond 1979).

We found that at shock velocities up to ~60 km/s, and for resolutions of 1024 cells in the direction of shock propagation + 2 levels of AMR (which gives a maximum resolution of 4096 cells), the agreement for the post-shock conditions between the 1-D code and AstroBEAR was mostly acceptable for the higher resolution run. Figure 13 shows test results for 60 km/s. This agreement began to break down as shock speeds approached ~80 km/s. However, we did not consider how physical scales affected the cooling. The length scale for the previous cooling tests was 200 AU, so that with 4096 cells, each cell spanned 7.30 x 10^{11} cm. The length scale for the current simulations,

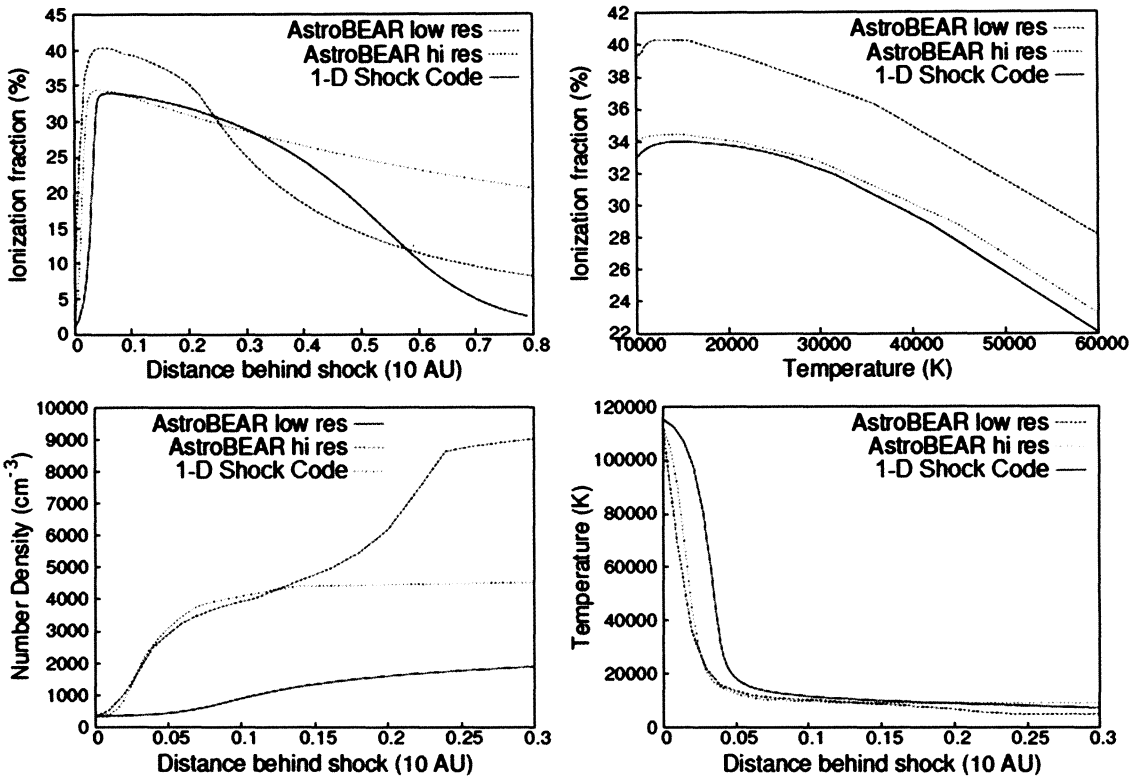

Figure 13: Post-shock and cooling zone values for X_H, n, and T for a 60 km/s shock. High resolution values for X_H and T match fairly well with the 1D shock code output, though T drops too rapidly. Number density does not agree well. (Carver 2010)

based on the size of HH 29 (roughly 800 AU) and allowing for space for the jet to develop and sweep over the clumps, ranged initially from 4000 – 8000 AU. This meant that even with the same numerical resolution, physically the shock would be 20 – 40 times less resolved. This was especially a problem given that shock velocities are ~80 km/s or higher.

To confirm that we had a problem, we looked at the post-shock conditions for simulation of a shock overrunning a single clump (see section 4.4 for the basic simulation set up). As is visible in Tables 1-4, the simulations with a large physical scale, even at higher numerical resolutions, do not even come close to the required post-shock values.

Temperatures, for example, barely get over 1/3 the expected value. The problem is that in the distance covered between timesteps, cooling occurs, driving down the temperature while increasing the density and the initial ionization fraction. One concern here is that if the post-shock temperature is not high enough, there will not be enough collisional excitation to give the bright Hα rims we see. This is probably not a problem for the higher resolution bow shock, which reaches a T_{PS} of ~50000 K (which is still far below the expected 140000 K), but the bow shocks in the clumps are from lower shock velocities, and there will be noticeable differences in the emission from a T_{PS} = 15000 K compared to what we should get at T_{PS} = 25000 K.

A few trends stand out in Tables 1-4. When looking at both the bow shock and clump shock values (Tables 2 and 3 respectively), we notice that the post-shock results all improve as resolution improves. They are acceptable by simulation #7 (2.28e11

Simulation #	Base cell size (cm)	# of AMR levels	Maximum numerical resolution (cells)	Maximum physical resolution (cm/cell)	Scale	Clump Radius (cm)
1	2.34e14	2	2048 x 512	5.84×10^{13}	1	7.47×10^{15}
2	2.34e14	3	3072 x 1024	2.92×10^{13}	1	7.47×10^{15}
3	2.34e14	4	6144 x 2048	1.46×10^{13}	1	7.47×10^{15}
4	1.17e14	4	12288 x 1096	7.3×10^{12}	1	7.47×10^{15}
5	7.30e12	2	2048 x 512	1.83×10^{12}	1/32	2.34×10^{14}
6	3.65e12	3	4096 x 1024	4.57×10^{11}	1/64	1.17×10^{14}
7	3.65e12	4	8192 x 2048	2.28×10^{11}	1/64	1.17×10^{14}
8	4.57e11	3	4096 x 1024	5.71×10^{10}	1/512	1.46×10^{13}
9	5.71e10	3	4096 x 1024	7.13×10^{9}	1/4096	1.83×10^{12}
10	7.13e9	3	4096 x 1024	8.92×10^{8}	1/32768	2.28×10^{11}

Table 1 - Resolution and scale information for the ten simulations to be compared.

Simulation #	v_{BS} (km/s)	$T_{PS, Expected}$ (x 10^3 K)	$T_{PS,Simulation}$ (x 10^3 K)	$n_{PS, Expected}$ (cm^{-3})	$n_{PS, Simulation}$ (cm^{-3})	$v_{PS, Expected}$ (km/s)	$v_{PS, Simulation}$ (km/s)
1	77.2	135	35.8	400	313	57.9	31.8
2	78.5	140	39.0	400	253	58.9	27.2
3	78.2	139	42.1	400	241	58.7	26.4
4	79.4	143	55.6	400	294	59.5	36.9
5	79.5	144	69.1	400	411	59.6	45.8
6	80.7	148	102	400	355	60.5	48.8
7	80	145	127	400	297	60.0	56.6
8	81.8	152	150	400	394	61.3	60.8
9	98.8	222	224	400	395	74.1	74.4
10	101	231	235	400	383	75.6	75.6

Table 2 – Expected post-shock values for the initial bow shock and resultant values from simulations.

Simulation #	v_{BS} (km/s)	$T_{PS, Expected}$ (x 10^3 K)	$T_{PS,Simulation}$ (x 10^3 K)	$n_{PS, Expected}$ (cm^{-3})	$n_{PS, Simulation}$ (cm^{-3})	$v_{PS, Expected}$ (km/s)	$v_{PS, Simulation}$ (km/s)
2	33.7	25.9	12.9	20000	22864	25.3	18.5
3	32.5	23.9	13.8	20000	17156	24.3	17.5
6	34.8	27.5	21.7	20000	21207	26.1	24.3
7	34.3	26.8	23.5	20000	20350	25.8	24.8
8	37.3	31.5	28.4	20000	20434	27.9	26.8
10	42.3	40.5	40.5	20000	17958	31.7	30.2

Table 3 – Expected post-shock values for the clump shock and resultant values from simulations.

cm/cell), and after #8 improvement is minimal to negligible. For the reverse shock (Table 4), however, things are a bit different. The temperature and density follow the same basic pattern (actually overshooting expected values in the smaller scale simulations). The post-shock velocity also looks like it is going to converge, but this

Simulation #	v_{BS} (km/s)	$T_{PS,\ Expected}$ (x 10^3 K)	$T_{PS,Simulation}$ (x 10^3 K)	$n_{PS,\ Expected}$ (cm^{-3})	$n_{PS,\ Simulation}$ (cm^{-3})	$v_{PS,\ Expected}$ (km/s)	$v_{PS,\ Simulation}$ (km/s)
2	69.5	110	21.9	4000	2181	17.4	48.5 (22.6)
3	70.5	113	25.2	4000	2216	17.6	46.3 (17.3)
6	68.2	106	45.4	4000	2573	17.0	38.9 (18.6)
7	69.6	110	54.7	4000	3110	17.4	34.8 (19.0)
8	70.9	114	86.6	4000	4295	17.7	21.1 (15.7)
10	77.3	136	143	4000	4117	19.3	10.2

Table 4 - Expected post-shock values for the reverse bow shock and resultant values from simulations. Numbers in parentheses are the v_{SH} values for one time step later.

time starts out too high, and decreases at finer resolution. This reversed direction is due to the fact that it is a reverse bow shock, and we are looking at slowing down the jet material, instead of accelerating the ambient material, as was the case for the forward bow shock. At lower resolution the post-shock densities are not large enough, so it makes sense that the incoming jet material is not decelerated enough, just as low densities had trouble accelerating the ambient material in the forward shock. As the reverse bow shock density increases (and overshoots), v_{PS} decreases to approximately the expected value, before it too overshoots. Figure 14 shows plots of temperature, T, and Hydrogen ionization fraction, X_H, for the different resolutions and scalings.

One note about simulation #10 is that the reverse bow shock structure does not follow the simple shape we expect. For example, for temperature, we expect a very sharp rise, followed by immediate cooling and decreased temperatures. What we see instead is a sharp increase to approximately the expected value, followed by a slower rise to a higher T, before then falling off, as seen in Table 5. If in Table 5 I had chosen the point where T = 136000 K as my post-shock beginning, then n_{PS} = 3990 cm^{-3}, and v_{PS} = 18.8

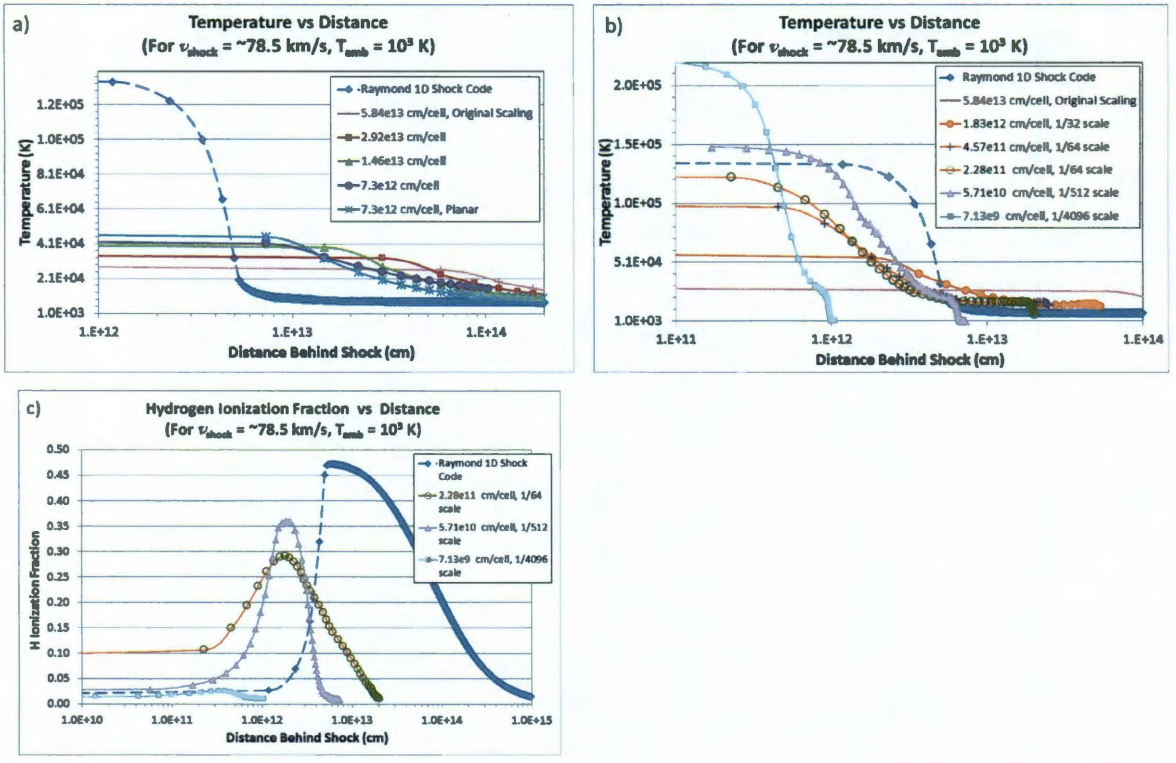

Figure 14: Shows effects of numerical and physical resolutions on post-shock temperatures (of bow shocks before they hit the clump), T_{PS}. Resolutions listed in the legends are maximum resolutions (AMR is taken into account). a) The original scale at varying resolutions is plotted (solid lines) along with the results from the 1-D shock code (dashed line). Higher numerical resolution improves their T_{PS}, but it becomes too computationally expensive to continue increasing that value. b) Simulations at smaller physical scales (hence higher physical resolution) are compared with the 1-D code. c) Hydrogen ionization fraction vs. time for some of the simulations from (b). Because of the reduced physical scale, the time scales for this shock speed are short enough for simulation 10 (light blue) that the shock does not have enough time to ionize properly.

km/s, both of which agree with the analytical values quite well. However, since the temperature continues to rise beyond this position, I chose the point of maximum T for my shock front instead.

Overall, it seems that decreasing the physical scale of the simulations in order to improve physical resolution does help to capture the shock and subsequent cooling zones properly. However, there are a few potential problems with this method that need to be avoided. One must keep in mind that the astrophysical jets have been flowing for at least hundreds of years (approximately 1200 years in the case of HH 29). This means that the

Distance To Shock Front (cm)	Temperature (K)	Number Density (cm-3)	v_{ps} (km/s)
3.66E+10	1002.1	1000.0	77.4
3.57E+10	1006.6	1000.4	77.4
3.48E+10	1714.9	1022.7	76.9
3.39E+10	36603.6	1483.5	62.3
3.30E+10	114601.0	3125.1	29.7
3.21E+10	134572.2	3927.5	20.0
3.12E+10	135626.7	3975.1	19.3
3.03E+10	135648.4	3975.6	19.1
2.94E+10	**136018.5**	**3990.5**	**18.8**
2.85E+10	136131.1	3993.1	18.6
2.68E+10	136717.5	4011.2	18.1
2.50E+10	137180.0	4020.5	17.6
2.32E+10	138042.7	4041.9	16.9
2.14E+10	138313.0	4032.2	16.6
1.78E+10	139456.0	4038.5	15.7
1.43E+10	140835.2	4046.4	14.5
1.07E+10	141686.2	4038.2	13.6
7.13E+09	143200.0	4079.2	12.2
3.57E+09	142801.9	4055.3	11.6
0	**143197.0**	**4117.2**	**10.2**

Table 5: 'Pre-shock' values for the reverse shock of simulation #10. The last entry was chosen as the shock front due to the temperature reaching its maximum value at that position. The other bolded entry is upstream of the chosen shock front. Its number density and velocity match the analytic post-shock values better, but since the temperature had not peaked, it was not chosen as the shock front.

shock has had time to reach steady-state, its cooling zone is fully extended, and the conditions behind the shock are stable. As the physical scale of simulations is decreased, this set-up may not be met. This seems to be the case for simulations #9, as seen in

Figure 14(b), and in #10. The lack of extended tail behind the sharp T drop, plus the second quick drop down to jet values, indicates that the shock is nowhere near steady state. Figure 15 shows the change in the cooling zone density over time for the bow shock for simulations #7 and #10. The cooling zone does not change much in #7, suggesting it is not changing extensively, whereas #10 is still growing significantly by the time it reaches the clump. Timescales here are approximately 95 days for #7, and only 0.19 days for #10, and size scales are 512 times smaller for #10 than for #7. The development of the cooling zone is particularly important when the shock overruns the clump. In order for the emission to match observations, we need the cooling zone structure to be as close as possible to the astrophysical case, where the shock propagating

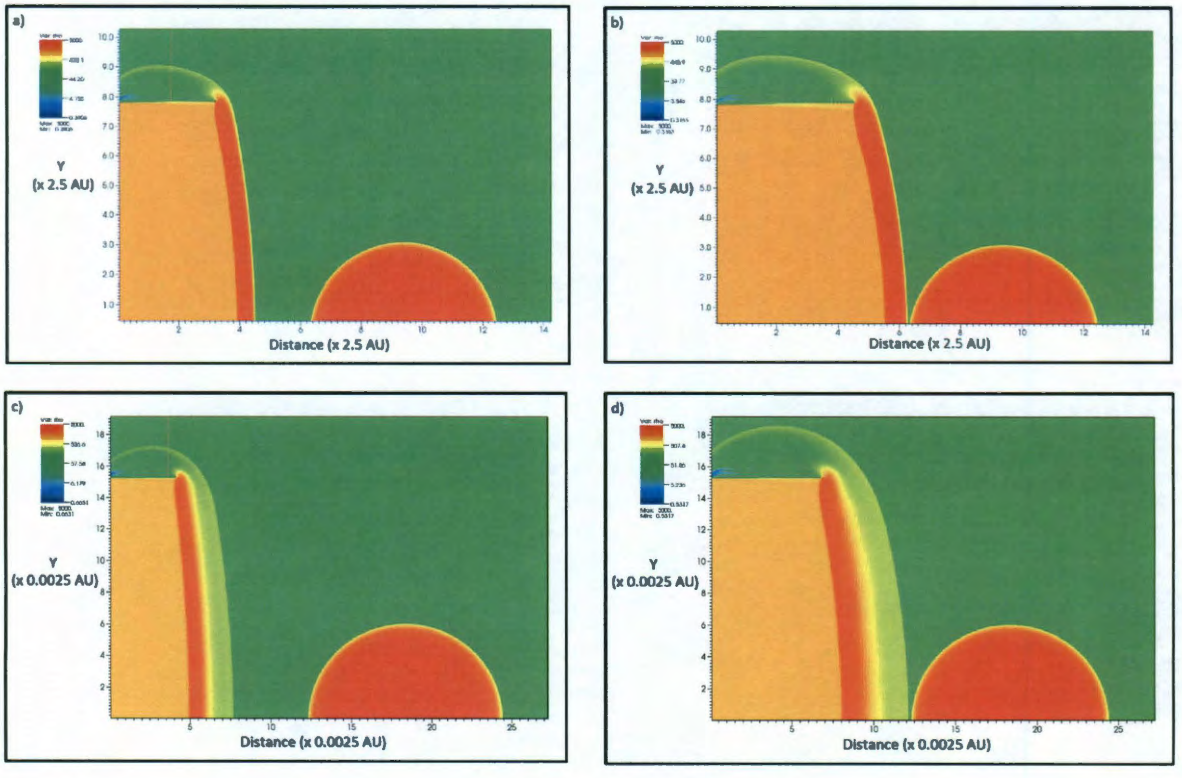

Figure 15: (a,b) Show the bow shock of simulation #7 over 4 time steps (from day 238 to day 333). There is little growth in the width of the bow shock. (c,d) show the bow shock of simulation #10, also over 4 time steps (from 0.333 days to 0.524 days). This bow shock is clearly far from steady-state, and is still growing rapidly in width as it hits the clump.

into a clump the size of those in HH 29 will fully develop before passing completely through it. Therefore, we want our clumps to be larger than a cooling length, $L_{cool.}$, and enough cells per clump to capture the cooling properly. From Yirak et al. 2010:

$$L_{cool} \approx \beta \frac{v_s^4}{\chi^2 n_c}, \tag{4.1}$$

where $\beta = 6.61 \times 10^{-11} cm^{-6} s^4$, v_s is the shock velocity, $\chi = \rho_{clump,initial}/\rho_{ambient,initial}$, and n_c is the clump number density.

4.4 - Single Clump Overrun by Jet

To examine a single shocked clump, the simulation was set up as in section 4.2, but with a clump added. The results of section 4.3 suggest that using the scale and resolution of simulation #8 are acceptable. The reverse bow shock T_{PS} is perhaps a bit low (86600 K instead of 114000 K, approximately 24 % low), but the other values are all

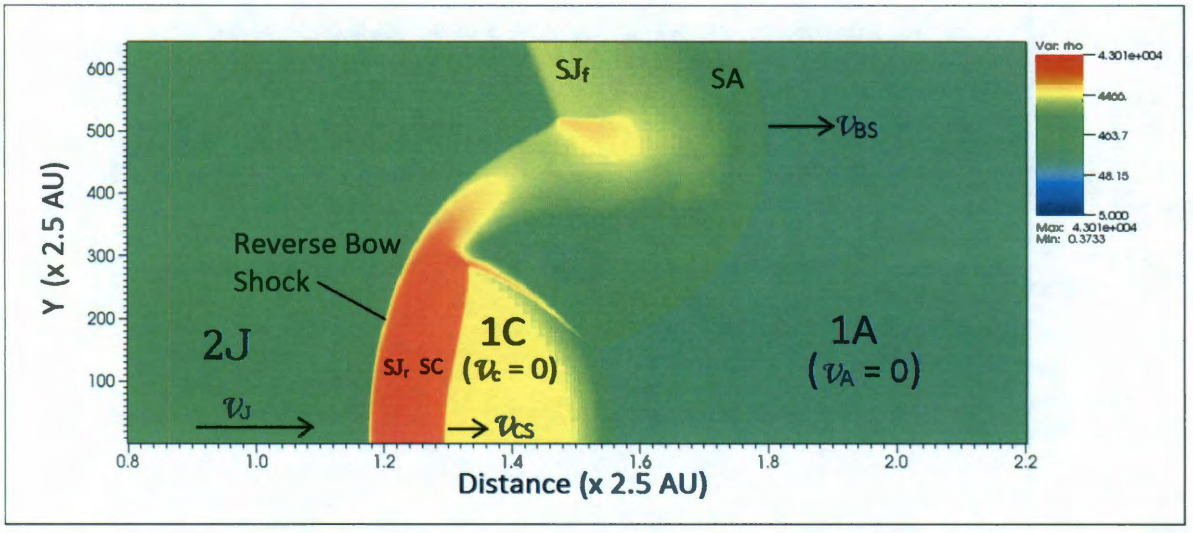

Figure 16: Density image of a shocked clump. The components drawn in Fig 6 are shown here: ambient material is 1A; shocked ambient is SA; jet material is 2J; shocked jet is SJ_f for forward bow shock and SJ_r for reverse bow shock; clump material is 1C; shocked clump is SC.

in very good agreement with calculations, and we do not seem to have reached the problem of the physical scale being too small yet. The clump in this case has the properties: T_{clump} = 100 K, n_{clump} = 5000 cm^{-3}, v_{clump} = 0 km/s, R_{clump} = 0.98 AU (1.46 x 10^{13} cm), and $X_{H,clump}$ = 0.01. The clump was placed 2.9 AU in from the left edge to allow the jet to form a bow shock before running into the clump, with a $v_{shock} \approx$ 80 km/s. Equation (4.1) then yields a cooling length L_{cool} = 2.2 x 10^{10} cm. This value is smaller than R_{clump}, though not larger than the cell size, indicating that some cooling will still occur within the cell (probably the cause for the low T_{PS}). Figure 16 shows a density image of the jet colliding with the clump for this set-up and labels the different components of the bow shock, reverse shock, and clump shock as drawn in Figure 6(b).

4.4(a) – Emission

The post-shock values found for simulation #8 in section 4.2 suggest that, given correct cooling routines, the emission we calculate with the post-processing methods described in sections 3.3a and 3.3b should be correct. The intensities were spot checked with hand calculations with their T, n_e, and X_H values and were found to match expectations, indicating the emission routines are implemented correctly. Therefore, to check that the cooling and shock-clump interaction are occurring as we expect, we want to look for features mentioned in section 1.3b, particularly the Hα and [SII] separation, the presence of a reverse bow shock with the separation as well, and a large velocity spread at the apex of the reverse bow shock.

Figure 17(a) and (b) show intensity maps of Hα (in red) and [SII] (in green) for simulation # 8 when the shock is approximately halfway through the clump (the same time in the simulation as Figure 16. This simulation was in 2.5D, but the single cell depth is 5.71 x 10^{10} cm, and this value was multiplied by the emissivity (erg cm^{-3} s^{-1} str^{-1}) to get an intensity (erg cm^{-2} s^{-1} str-^{1}). Figure 17(a) displays the expected bright Hα at the edges of the forward and reverse bow shock from collisional excitation due to the high post-shock temperatures. As the temperature decreases, we see emission from collisionally excited [SII], and more Hα from recombination. Figure 17(b) zooms in on the reverse bow shock and the clump shock. The differences between the two shocks stand out here, where we note that the clump shock does not have an obvious collisional excitation rim. Instead it has [SII], with Hα appearing right behind it. The post-shock temperature of this shock is about 30000 K, which should be enough to begin to collisionally excite H, and indeed it does. The Hα we see is due to collisional excitation, and begins approximately where I have defined the shock front in Table 1. However, because the shock front is not infinitely thin, and there are a few cells over which the shock builds up, as the temperature increases we get some collisionally excited [SII] before the temperature is high enough to collisionally excite H. Between the clump and reverse bow shocks, the green [SII] emission seems to dominate, but that is due to their relative maxima. Figure 17(c) shows Hα minus [SII], and we see here that Hα still dominates in that region (though not by much). What is not obvious in Figure 17(c) is that in the region labeled [SII], the values are negative, and [SII] actually mildly dominates.

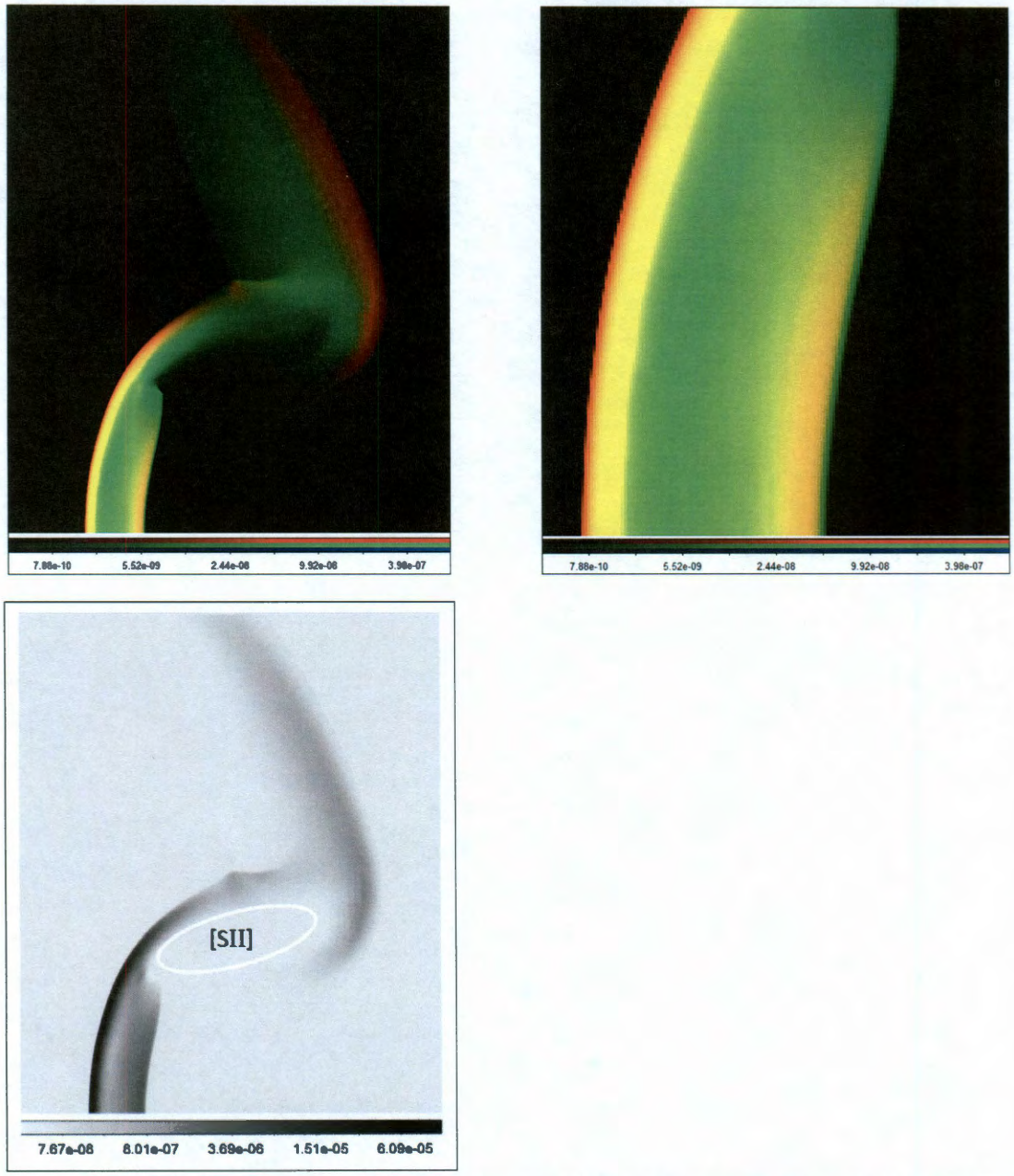

Figure 17: a) Hα (red) and [SII] (green) for simulation #8. b) Same as (a), zoomed in on the reverse bow shock (RBS) and clump shock (CS). The RBS shows Hα along its edge due to collisional excitation. The CS has a [SII] edge, suggesting the temperatures (~ 30000 K) are too low to collisionally excite much Hα. c) Hα minus [SII], showing Hα dominates everywhere except in the encircled region labeled [SII].

To look at radial velocities, I ran a one clump simulation in 3-D and separated the Hα emission into 3 radial velocity bins, similar to Figure 3. The bins, with negative velocities being toward us and positive away, are v_{radial} = 30 to -10 km/s (red; mostly

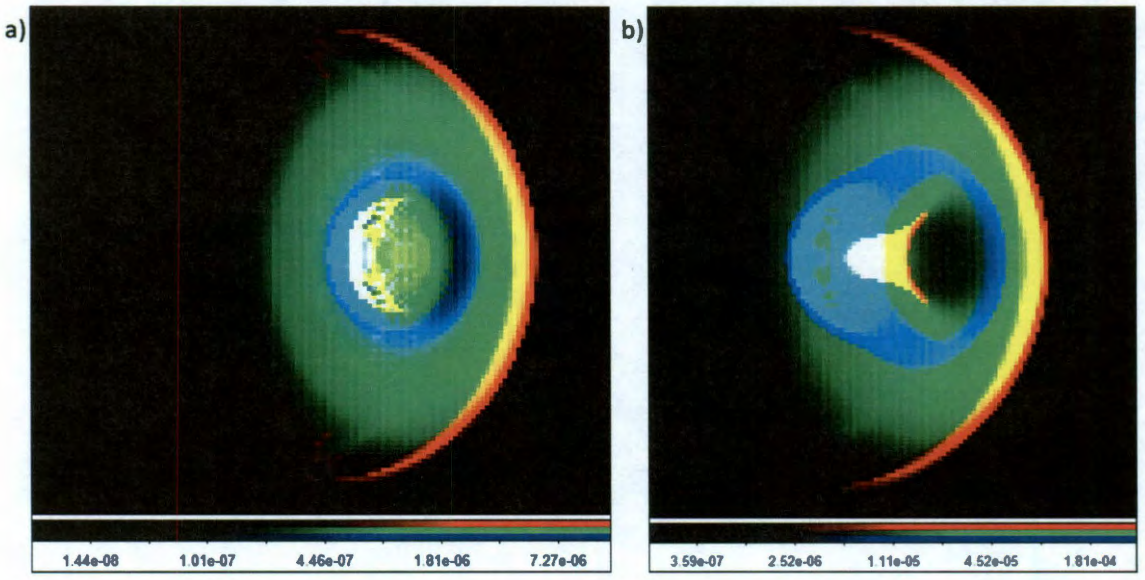

Figure 18: RGB color composite radial velocity map of Hα for a jet overrunning a single clump, with the jet oriented 45° toward us. Velocity bins, in km/s, are Red: 30 to -10; Green: -10 to -50; Blue -50 to -90, where negative velocities are toward us. R+G gives yellow, and R+G+B gives white. We see white at the apex of the reverse bow shock, indicating material is flowing around it in all directions. (b) is a later time frame of the same simulation as (a). This simulation was done at 1/64 scale, but only 7.3×10^{12} cm/cell.

away), -10 to – 50 km/s (green; somewhat toward us), and -50 to -90 km/s (blue; rapidly toward us). The bins were chosen this way because I have also angled the jet toward us at 45°, similar to HH 29's angle of 47°. Figure 18 shows the velocity map for this simulation when the shock is approximately halfway through the clump. We see that we get the largest spread in radial velocities, with all three colors yielding a white color, at the apex of the reverse bow shock.

4.4(b) - Variations for 1 Clump

The presence of a magnetic field can have a drastic effect on the morphology of the flow. Figure 19 shows three 3D simulations: (a) has no magnetic field but includes full cooling and particle tracking; (b) also has no magnetic field but has only the original

Dalgarno-McCray cooling (does not track N_e or X_H); (c) has a magnetic field in the y-direction of about 0.4 mG ($\beta_{plasma} = 10$) and also has only the DM cooling. The reason for the cooling differences is that AstroBEAR cannot currently implement both a magnetic field and full cooling; however, it can use its original DM cooling with a magnetic field. This will allow us to compare morphologies and dynamics with a non-magnetic simulation, though without the full cooling (which tracks N_e and X_H), we cannot calculate line emission for direct comparison with observations or non-magnetic simulations.

The DM cooling routine cools a bit less than the full cooling routine, and is a bit more puffed out, but the overall shape is for the most part quite similar. This means that differences between (c) and (a) can be attributed almost exclusively to the presence of a magnetic field in (c). The magnetic field in (c) is aligned in the y-direction, which resists changes in the plasma in the x-direction, making it much harder to compress in the post-shock region. β_{plasma} is the ratio of the gas pressure to the magnetic pressure, $\beta_{plasma} = P_{Gas}/P_B$, and the value used here, $\beta_{plasma} = 10$, means that the magnetic field is not very strong. Even so, the effect on the dynamics is quite drastic. We see from the early frame of (c) that the bow shock is much more puffed out than the bow shock of (a) or (b), and that by the time its main bow shock has begun to interact with the clump, its diffuse bow shock has already swept past the clump. The region between the clump shock and reverse bow shock is mildly less dense in (c) than in (a), but it is also more extended. This is due to the extended diffuse bow reaching the clump early and beginning to compress the clump before the non-magnetic cases have even reached the clump. Further studies will have to be done to determine how much of this is a resolution effect and how much is

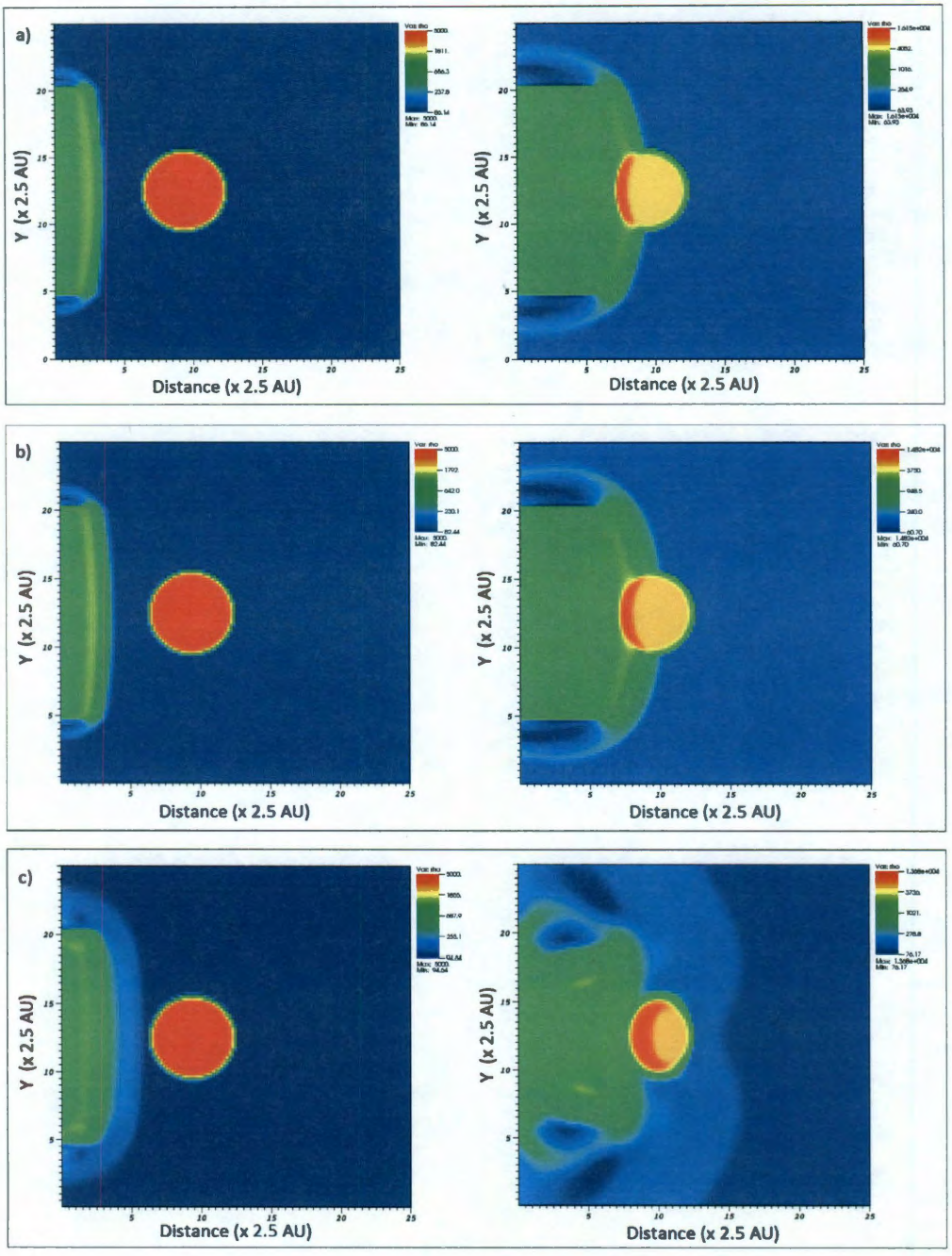

Figure 19: 3D non-magnetic and magnetic simulations (a) Non-magnetic, full cooling with particle tracking. (b) Non-magnetic with the original Dalgarno-McCray equilibrium cooling. (c) Magnetic with $B = B_y \sim 0.4$ mG, and DM cooling. The magnetic field adds pressure support to the post-shock region, and prevents the kind of compression seen in the non-magnetic runs.

purely due to the magnetic field. We should note that the jet in this simulation has a H ionization fraction of 0.01. A more neutral jet would be less affected by the field, and a more ionized jet would be more affected by the field.

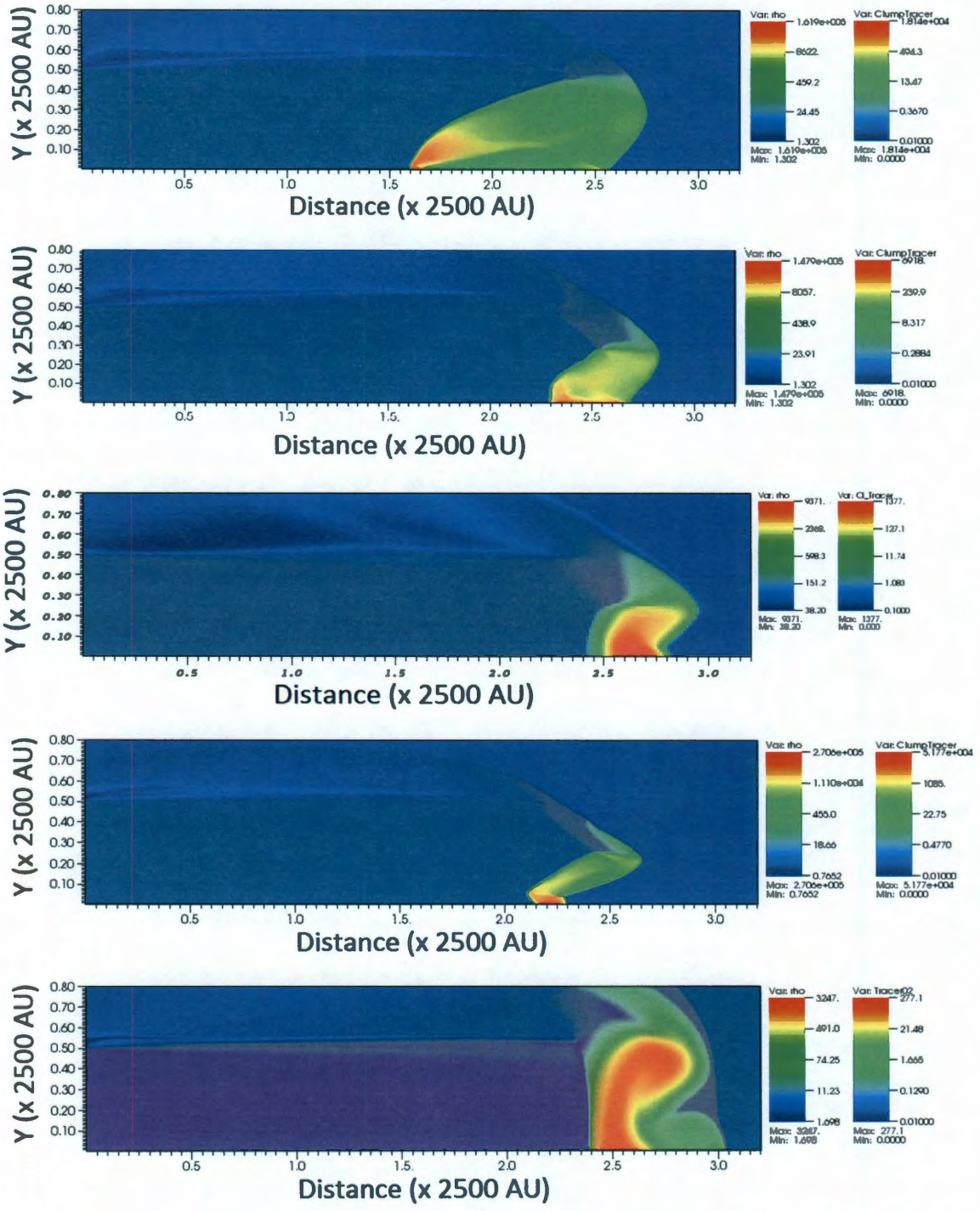

Figure 20: Shock overrunning a single clump. a) $n_{clump} = 5n_{jet}$; b) $n_{clump} = n_{jet}$; c) $n_{clump} = 0.5\ n_{jet}$; d) Mach 50 jet ($v_{jet} \approx 200$ km/s); e) No cooling.

We also briefly look at the effect of clump density in these simulations. Figure 20 shows three cases: a) $n_{clump} = 5\ n_{jet}$ (as all of the above simulations are); b) $n_{clump} = n_{jet}$;

c) $n_{clump} = 0.5\ n_{jet}$. Note that the maximum temperature for (c), the least dense clump case, is lower than the other two cases. This suggests that, for the proper shock velocity, we might get [SII] emission without collisional Hα for lower density clumps. Because the less dense clumps are more easily accelerated, they are less likely to get smeared out. Figure 20 shows that the densest clump is actually smeared out more, since more jet material is forced to flow around it during its slower acceleration. This leads to more extended emission regions as well.

4.5 – HH 29: Basic Set-up of Simulation

Rather than attempt to model all nine clumps labeled by Devine et al. in their image of HH 29 (Figure 2), my goal in this section is to model some of the basic components of HH 29. To that end, I chose four clumps to model: I, B, D, and A, as shown in Figure (b). This simulation is done at the original physical scale instead of the smaller scale used for the single clump simulations. Ambient conditions are: $n_{amb} = 100$ cm^{-3}, $T_{amb} = 1000$ K, $v_{amb} = 0$ km/s, and $X_{H,amb} = 0.01$. All clumps are of the same size, density, temperature, and ionization fraction: $R_{clump} = 250$ AU (3.74×10^{15} cm), $n_{clump} = 100\ n_{amb} = 10^4$ cm^{-3}, $T_{clump} = 10$ K (set from pressure balance with ambient) , and $X_{H,clump} = 0.001$. The jet conditions are: $n_{jet} = 10\ n_{amb} = 10^3$ cm^{-3}, $T_{jet} = T_{amb} = 1000$ K, and $X_{H,jet} = 0.01$. The simulation is 3D and the computational grid is 64x32x32 (8000x4000x4000 AU) with two levels of AMR, yielding a resolution of 4.675×10^{14} cm/cell. While this is not high enough resolution to fully resolve the shock (see section 4.3), the output will be enough to begin exploring the parameter space for HH 29. The placement of the clumps

involves a large amount of guesswork, since the 2D projection of the observations provides no details on relative depths of the features observed.

The shock and jet speeds here are the same as for the 1-D simulations, which are less than those found for HH 29. Recall from the analysis of line widths by (Stocke et al. 1988), that $v_{shock} \sim 190$ km/s. If we were to use that shock speed, we would not be able to increase the resolution enough to capture the post-shock values correctly, and our emissions would not be valid. As it is, direct comparison of fluxes, due to the different shock speeds, cannot be done, but as a basis for exploring the parameter space of HH29, $v_{shock} = 80$ km/s is fine.

4.5(a) - Comparison of emission with observations

Figure 21 (a) shows an Hα and [SII] composite image of this simulation when the shock has just overrun clump D', where the prime indicates that the clump from the simulation is associated with clump D from Figure 2. The 3D output has been rotated 45° toward us, and the emission summed up along the line of sight to yield the intensity map shown in the figure. We can see some obvious similarities, as well as many areas that do not match. In terms of clump placement, clump B' needs to be further to the right, as does clump I', but they are not too far off. Clump I' has been hit by the wing of the bow shock in the simulation and is more smeared out than observed. It also creates a gap that appears to be moving up and to the right as the bow shock continues past (the bow shock is still expanding as it moves). Clumps A' and D' appear somewhat relatively brighter than their observed counterparts, though the shape of the reverse shock of clump

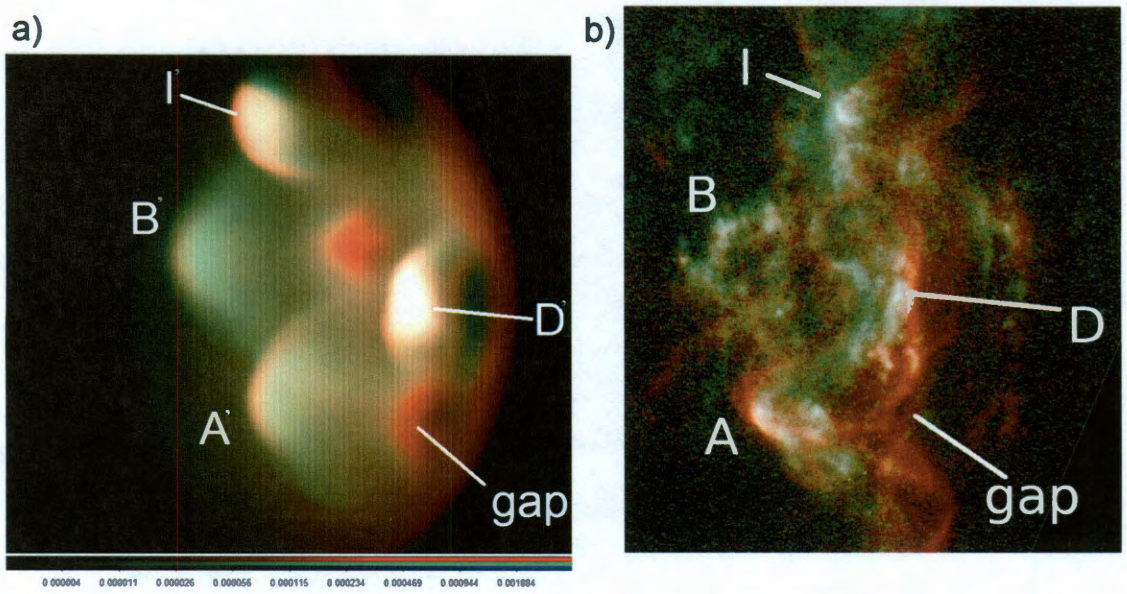

Figure 21: a) Intensity map from a simulation with four clumps, rotated 45° to match the view of HH 29. b) Zoomed in view of HH 29 (Devine et al. 2000). In both images, red is Hα emission, and [SII] is shown in green + blue. Clumps in the simulation have been labeled with primes for clearer reference.

A' bears a good match to that of clump A. D is not clearly a clump in the observation, having no apparent reverse bow shock. It is not surprising that modeling it as a clump has produced more of a reverse bow shock than desired. There is some Hα and [SII] separation at D, however, and that is produced by D'. Additionally, neither B nor I show an Hα rim the way B' and I' do. Possibly these clumps were moving in the direction of the jet, reducing the shock speed enough that very little Hα due to collisional excitation was produced.

Major differences between simulation and observation are the lack of the noticeable gap behind A', and the presence of a gap behind clump B'. There is a gap behind A', but due to the angle of the jet, this gap is masked by the emission from the far side of the jet. Placing A' on the far side of the jet may perhaps reduce this problem. As for the gap due to clump B', this is again due to the jet's angle, as there is not enough emitting material behind or in front of the gap to mask it. It could be that clump B was

initially farther upstream, allowing the bow shock enough time to wrap around it and fill in the gap. Clearly clump placement needs to be more fully explored to constrain the possibilities.

Figure 22 (a) and (b) show Hα – [SII] maps for the simulation and observations respectively. Unlike the composite image of Figure , here there are almost no similarities. The observations indicate that [SII] dominates the top half of HH 29, whereas Hα emission dominates the lower half, and there is no clear evidence of clumps, or the separation of Hα and [SII] that the simulation shows. One of the main problems of this particular simulation is that due to the low resolution, the jump conditions are not correctly met and the post-shock temperatures are far lower than expected. As discussed in section 4.3, this has the effect that very little H is collisionally excited, and yielding only small amounts of Hα immediately behind the shock. As is evident in Figure 22(a), the Hα emission seems washed out, and even the rims show only mild Hα dominance. Increasing the resolution would produce more Hα emission. However, this does not

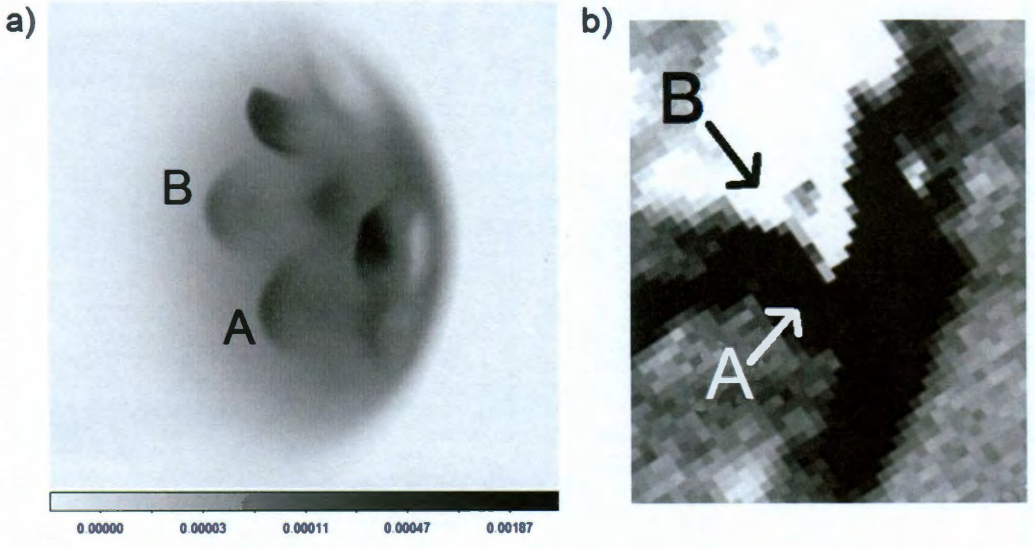

Figure 22: a) Hα minus [SII] image from simulation. b) Observed Hα minus [SII] image (Hartigan et al. 2000). Black shows Hα dominance and white indicates [SII] dominance.

explain the two large separate regions of [SII] and Hα observed. It is possible that this is partly due to the geometry of the bow shock. Our modeled bow does not sweep back as drastically as most observed bow shocks, so the wings are less oblique than expected. This means that shock velocities do not drop off as rapidly as they should, which would in turn lead to more Hα and less [SII] dominance. However, the bulk of the observed [SII] in Figure 22(b) is near the front of the bow shock, so this probably does not play a large role. Another possibility is that the material in the [SII] region was already moving in the direction of the jet when it was shocked, leading to lower shock velocities and higher [SII] to Hα ratio. The time difference image of [SII] in Figure 2 of (Devine et al. 1999) though does not indicate a noticeable difference between the upper and lower halves of HH 29 over time.

A radial velocity map of Hα from the simulation is shown in Figure 23(a), compared with a zoomed in version of the upper left panel of Figure 3, here labeled Figure 23(b). The velocity range chosen for the simulations is less than that chosen for the observations due to the fact that I am using a smaller v_{jet} and v_{shock} than those of HH 29. Although the resolution of the observations in (b) is much lower than the HST Hα and [SII] in Figure 2 and Figure 21(b), and individual clumps are more difficult to distinguish, we should still see the basic features of the observation in our simulations. The main observation, mentioned in section 1.3 and discussed in section 2.1, is the large spread in radial velocities at reverse shocks, where shocked and emitting gas is flowing around the clumps both toward and away from the observer at high velocities. We see in Figure 23(a) that simulated clump A does present a reverse bow shock with emission indicating both negative and positive radial velocities.

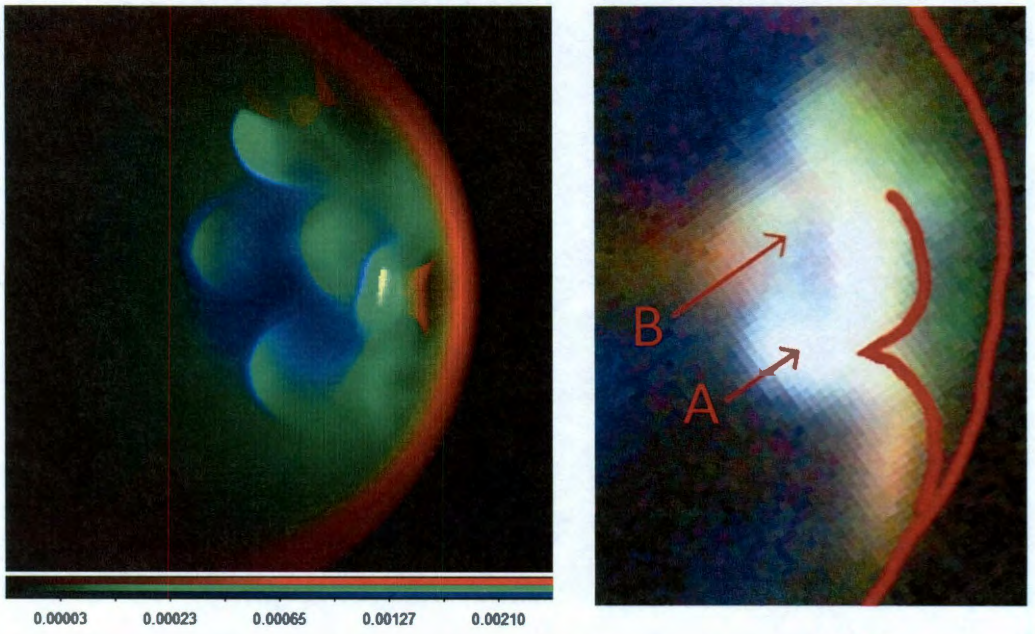

Figure 23: a) Hα radial velocity map from simulation the 4-clump simulation. Velocity bins are indicated by color: Red = +30 to -10 km/s (mostly away from observer); Green = -10 to -50 km/s (toward observer, medium speed); Blue = -50 to -90 km/s (toward observer, high speed) b) Same as (a) but from observations with a Fabry-Perot spectrometer, with the velocity bins: Red = +45 to -15 km/s; Green = -15 to -75 km/s; Blue = -75 to -135 km/s.

4.5(b) – A brief exploration of parameter space

Five main changes were made to the set-up described in section 4.5 to examine their effects on our model of HH 29, both kinematically and in terms of the emission line maps. These were: 1) reducing the density of the clumps; 2) doubling the speed of the jet; 3) changing the shape of the bow shock; 4) reducing the size of the clumps; and 5) adding a magnetic field. These simulations were otherwise identical to the set-up described in section 4.5, with the exception that they only used one level of AMR instead of two. Results are displayed in Figure 24 for the first 4 changes, which shows Hα (red) and [SII] (green) composites, and Figure 14 for the added magnetic field.

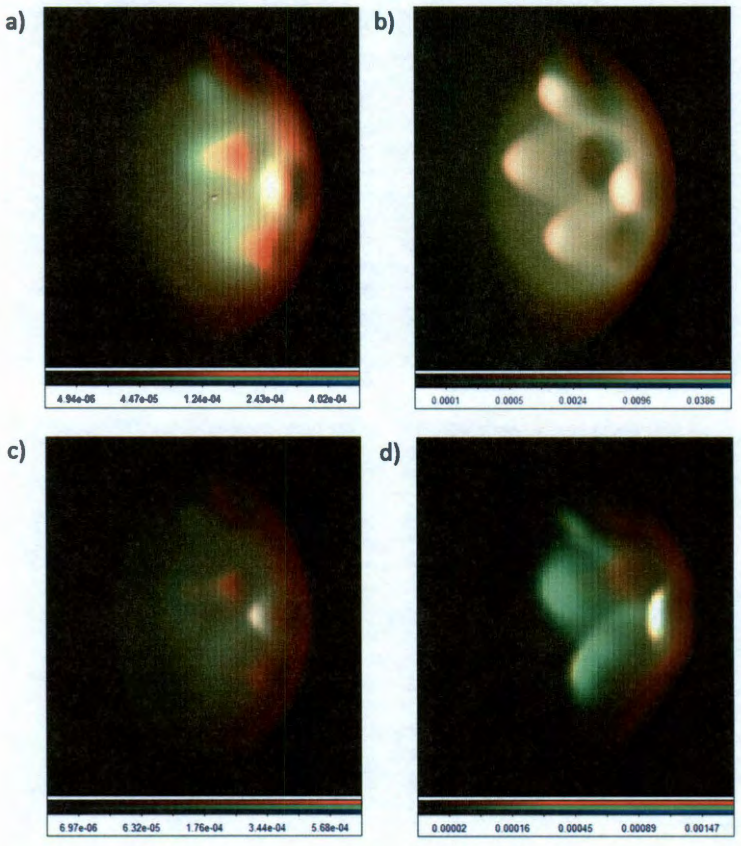

Figure 24: Hα (red) and [SII] (green) composite for simulations of 4 clumps. a) Clump density has been halved. b) Jet speed has been doubled (Mach 54) c) Clump radius has been halved. d) Shape of bow has been changed (by reducing jet speed away from its axis)

In the `Less Dense' simulation, the initial density of the clumps has been reduced by a factor of five and is equal to the jet density. As seen in Figure 24(a), the emission from the shocked clumps appears more diffuse than in the original simulation shown in Figure 21(a), and the maximum Hα intensity shown is a factor of about 4 less than the original. There are no obvious kinematic differences between these two runs, with the possible exception of the gap behind clump B closing more quickly in the `Less Dense' case. In both the composite image and the Hα minus [SII] image, the gap (shown as strong Hα) behind clump B is narrower and more elongated than in the original simulation.

The reverse bow shocks in the `Mach 54' simulation ($v_{jet} \approx 200$ km/s), Figure 24(b), are more pointy than in the original run. The positions of the clumps and gaps with respect to one another are all approximately the same as for the original speed, though if they had started out with larger separations, and images were taken at a later time, that would not be the case. The maximum Hα intensity is approximately twice that of the original simulation.

Figure 24 (c) shows the result for the `Small Clump' simulation, in which the clumps had half the radius as the original. As with the `Less Dense' simulation, the emission here is very diffuse, with a maximum Hα intensity approximately one-third that of the original simulation. Only clump D shines brightly, and it is much more localized than the original. The gaps behind clumps A and B are almost closed, resulting in a sideways `Y' shaped gap.

The last change that provides an intensity map is the run in which the jet velocity drops off to $0.4v_{jet}$ at its edge, rather than $0.8v_{jet}$ in the original run. I chose this simulation in the hope that the more oblique wings of the bow shock might yield a larger [SII] region, closer to what is seen in Figure 3 than the other simulations have achieved. As Figure 24(d) shows, however, this is not the case. The dynamics are greatly affected though, with the clumps now closer to the wings, they end up being more smeared out as the shock overruns them. The emission does not vary much from the original run, with the maximum Hα intensity being approximately the same. Clump A seems to have been a bit more compressed than in the original.

As mentioned in section 4.4(b), AstroBEAR cannot currently implement both a magnetic field and the full cooling routines in a given run. The old cooling routine,

which incorrectly assumes ionization equilibrium and does not track particles, must be used instead, which means we cannot produce emission line maps from simulations with magnetic fields. Instead, we can look at the kinematics of the simulation and how the magnetic fields affect the dynamics. We use a magnetic field in the y-direction, with a strength of approximately 0.4 mG.

Figure 25 shows comparisons of densities, with the left column being from the original simulation, and the right column including the magnetic field. In row (a), the clump densities are shown, along with magnetic field lines in the image on the right. The magnetic field gets bent toward the right by the jet, and in turn pushes the clumps to the right, into a sort of bow shock shape. The clumps are not as compressed at their front (shock) side, nor as stretched out behind them as in the non-magnetic simulation. The magnetic field appears to mitigate the effects of the shock and preserve the clumps in the x-direction. Not shown, however, is a view down the x-axis, which shows that the clumps in the magnetic field are getting smeared out in the z-direction instead, since the magnetic field lines are not being compressed by the jet in that direction. There is little difference between the two simulations in the y-direction. Row (b) shows the same two simulations but with contours of the total density added (and the field lines are no longer displayed). The jet and ambient densities are clearly affected by the presence of the magnetic field.

If we were able to obtain emission line maps for magnetic simulation, we would expect to see less of the higher excitation emission, and perhaps more of the lower excitation emission, relative to a non-magnetic run. Figure 25 clearly shows the reduced compression of the clumps, indicating a weaker shock than in an identical but non-

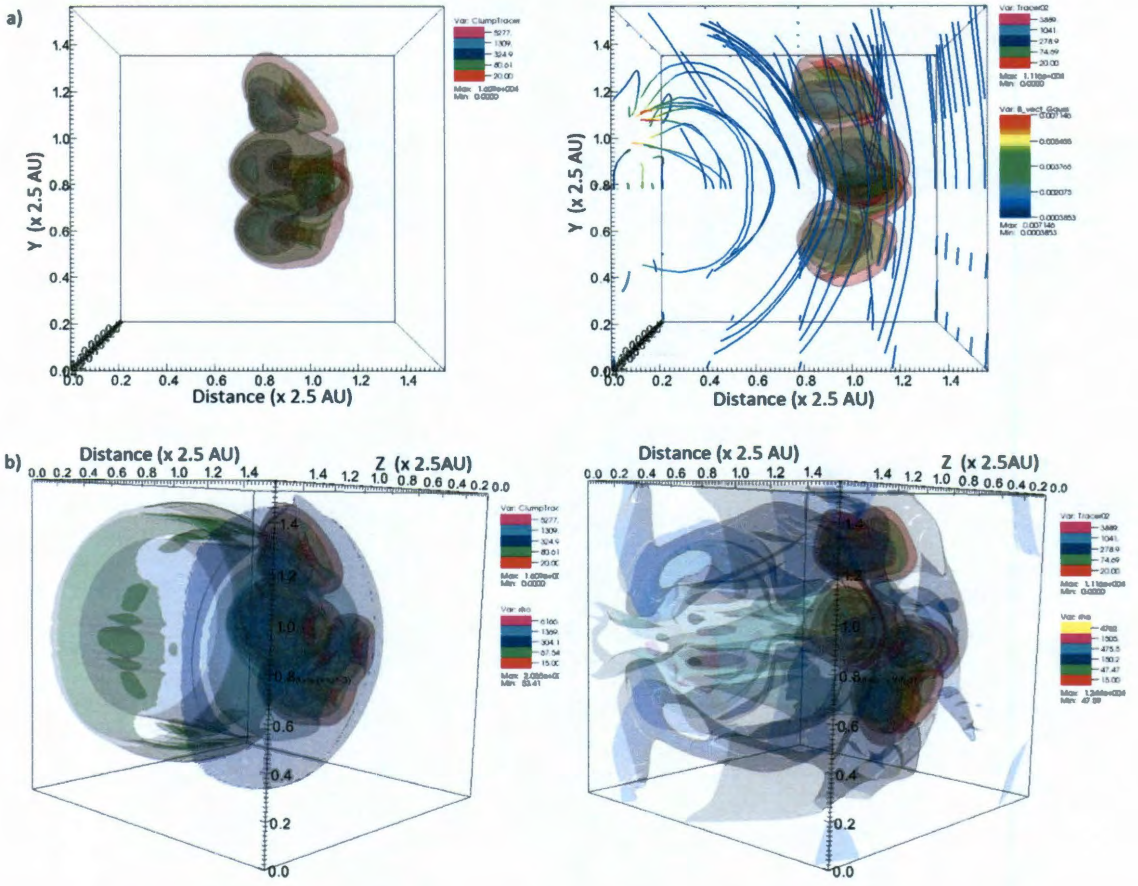

Figure 25 a) The left image is the clump density for a regular run, and the right image is the same but for a simulation with a magnetic field in the y-direction, with the lines representing magnetic field direction and strength.. b) Same images as in (a), but with total density displayed as well, and with the image rotated toward us. The magnetic field lines are not shown in the images on the right.

magnetic simulation.

One additional parameter that was not particularly explored in this work is clump position. Given the jet's angle of 45° toward the observer, positioning a clump on the near side of the grid (larger z-value) will make it appear farther to the left relative to mid z-plane when rotated, whereas positioning it toward the far side (smaller z-value) will make it appear farther to the right when rotated. The z-position will also affect the radial velocity maps. Emission from shocks will have smaller radial velocities behind and to the right of clumps due to the jet orientation, and larger radial velocities

Chapter 5

Relations to Laboratory experiments and simulations

Current laboratory experiments focusing on shocked clumps yield results that are very similar to what we see in HH 29 and other HH objects. The basic set-up for the shock-clump experiments is shown in Figure 26 for single clump trials. Multiple lasers are targeted on the inside walls of the hohlraum, heating them and increasing the temperature and thus pressure inside the cavity. This pressure blasts the CHBr into the CH and all into the Resorcinal-formaldehyde (RF) foam, creating a shock that propagates through the foam and overruns the clump. Trials with multiple clumps are set up in the same way, but with many, smaller clumps instead of the single clump. Images are taken

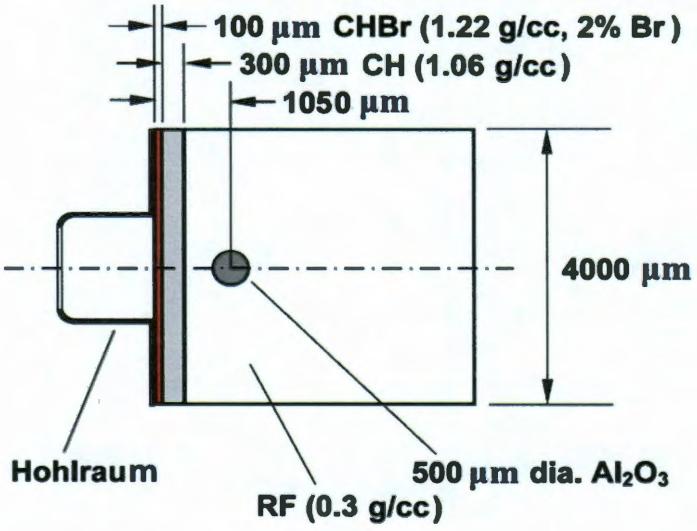

Figure 26: Set-up of single clump laboratory experiment. A laser is shone into the hohlraum which heats up and in turn heats the area within it. This creates a pressure drive that pushes the CHBr into the CH, and into the RF foam. This creates a shock that overruns the clump. Multiple clump versions use the same basic set-up, but have many, smaller clumps with which the shock interacts (Rosen et al. 2009)

by other lasers targeting backlighters which then emit x-rays that travel through the foam to a CCD and provide an x-ray image of the experiment at a single precise time.

Figure 27(a) shows a numerical simulation of a multiple clump laboratory experiment done on the RAGE code of Los Alamos National Laboratory (image provided Melissa Douglas). The shock propagates from left to right, and in the first image we see the shock approaching numerous small clumps (embedded in a denser RF foam). The second image shows the clumps after they have been fully overrun by the shock. We see reverse bow shocks around the many clumps, and a gap can be seen to the right of the clumps, as we expect as the shock is slowed by the clumps and forced around them, and

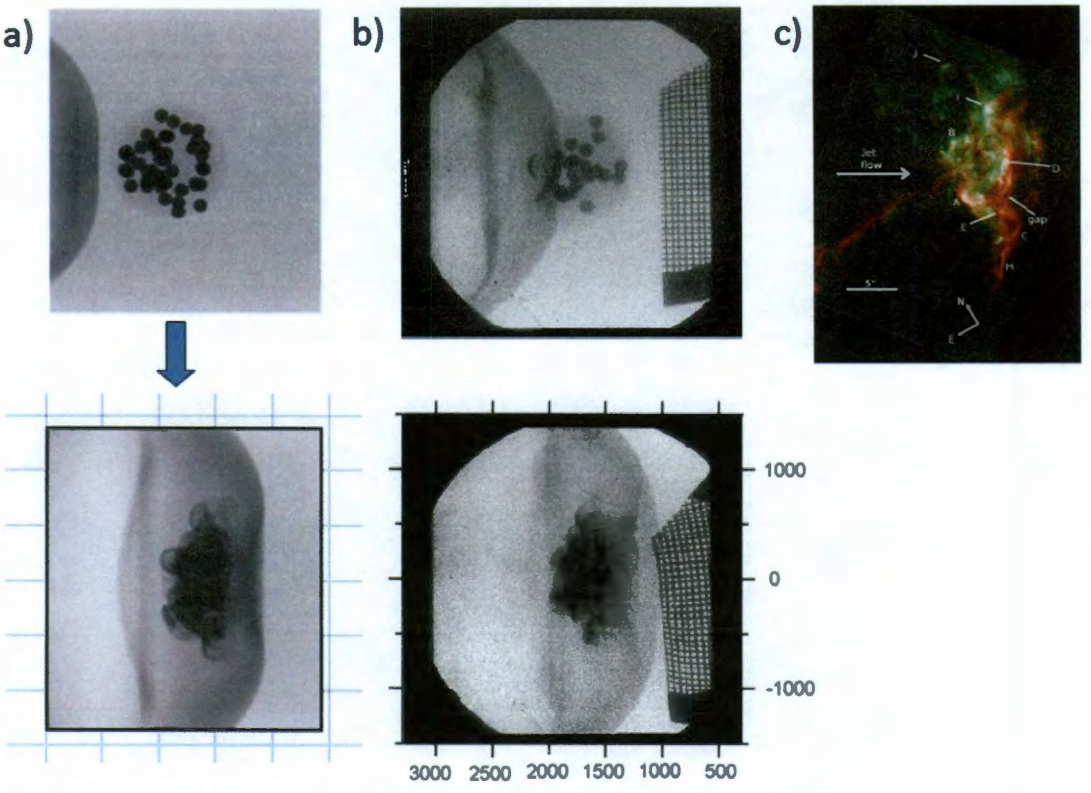

Figure 27: a) Simulated radiographs output from a multiple clump RAGE simulation of laboratory experiments. The shock moves from left to right. In the first image, the shock has not yet reached the clumps, and in the second image, the clumps have been overrun by the shock. b) Radiograph from a shocked clumps laboratory experiment. Note the reverse bow socks as the gap from the bow shock after it has flowed around the clumpy area. c) HH29, for comparison.

has yet to reconnect downstream. In Figure 27(b), a radiograph from the actual laboratory experiment is shown, which qualitatively agrees very well with the simulation. For comparison, Figure 27 (c) shows HH29. There are no emission lines from the experiment (or laboratory simulation) to compare, but the basic features (reverse bow shocks, gaps) are similar. The fact that the overall shape is also very similar is probably a coincidence.

Although we cannot compare these experiments directly to observations, the numerical simulations are an important bridge between the two. A laboratory simulation could be modeled that scales to observations and attempts to match a specific astrophysical object. If that object were also to be simulated with an astrophysical code, the two models could be compared. If the lab simulation agrees well with the lab experiment and also with the astrophysical simulation, which in turn compares favorably with the observations, then we have increased confidence that we are understanding the physics involved on both scales.

Chapter 6

Conclusion

The main goals of this thesis were to modify AstroBEAR to include the ability to create synthetic emission line maps, and to make sure its cooling routines function properly in realistic regimes. Using AstroBEAR to track electron and Hydrogen densities, we were able to calculate Hα intensities. We used charge-exchange to set the ionization fractions of oxygen and nitrogen, and solved for the level populations of each species (OI, OII, NI, NII, and SII) which allowed us to calculate their intensities. In order for the emission to be valid, the code had to deal with shocks and the post-shock cooling zones correctly. It had previously been found that the post-shock cooling structure of AstroBEAR failed at higher velocities. What we discovered in this work was that when the physical scales are too large, the numerical resolution required to resolve the cooling zones, i.e. to make cell size $\precsim L_{cool}$, is prohibitively large. One way to solve this problem is to shrink the simulated physical scales to the point where this criterion is met. However, with a physical grid that is too small, the shock will pass through the clump before it can reach steady state post-shock values. We adopted a compromise, shrinking the physical scale of the problem to the point where the cooling zones were almost resolved, but the overall grid size was not yet too small to allow the post-shock conditions to reach their analytical values. We simulated shocks overrunning single clumps and verified the cooling in the post-shock regions of the bow shock, reverse bow shock, and clump shock.

We chose to simulate HH 29 as a test bed for this new ability of AstroBEAR, both for the intrinsic features of HH 29 (it is close, large, and clumpy) and the fact that it has high resolution HST images of it, plus radial velocity maps from Fabry-Perot spectrometry. A brief exploration of the parameter space was conducted, including the effects of clump density, clump position, and shock speed on the emission, as well as the kinematic effects of a magnetic field. While no definite claim can be made on the correct set-up for HH 29, this work begins to constrain these parameters, and can provide a launch pad for future similar work on HH 29.

6.1 Future Work

The cooling routines in AstroBEAR discussed in section 3.2(d), for cooling at temperatures below 10^4 K, need to be implemented for these simulations. The lack of this low temperature cooling does not have a significant effect on the kinematics of a simulation, but will affect the emission we can see. AstroBEAR also needs to be able to include all of its cooling routines in MHD simulations. Without this capability, we will not be able to compare directly an MHD simulation with observations.

REFERENCES

Anderson, D. D., Dobbs, D. E. and Mullins, B. (2002). "Corrigendum: The primitive element theorem for commutative algebras (vol 25, pg 603, 1999)." Houston Journal of Mathematics **28**(1): 217-219.

Anderson, H., Ballance, C. P., Badnell, N. R. and Summers, H. P. (2000). "An R-matrix with pseudostates approach to the electron-impact excitation of HI for diagnostic applications in fusion plasmas." Journal of Physics B-Atomic Molecular and Optical Physics **33**(6): 1255-1262.

Bally, J. and Reipurth, B. (2002). "Recent Developments in the Study of Herbig-Haro Objects." Emission Lines from Jet Flows, Isla Mujeres, Q.R., México, November 13-17, 2000 (Eds. W. J. Henney, W. Steffen, A. C. Raga, and L. Binette) Revista Mexicana de Astronomía y Astrofísica (Serie de Conferencias) Vol. 13: 1-7 (2002) (http //www.

Cabrit, S., Ferreira, J., Dougados, C., Pesenti, N. and Garcia, P. (2005). The Origin of MHD Jets in T Tauri Stars. MAGNETIC FIELDS IN THE UNIVERSE: From Laboratory and Stars to Primordial Structures, AIPC.

Carver, R. L. (2010). Shocks and Jets from the Laboratory Environment to the Astrophysical Regime: Transforming AstroBEAR Into an All Purpose MHD Simulation. **PhD**.

Coker, R. F., Wilde, B. H., Foster, J. M., Blue, B. E., Rosen, P. A., Williams, R. J. R., Hartigan, P., Frank, A. and Back, C. A. (2007). "Numerical simulations and astrophysical applications of laboratory jets at omega." Astrophysics and Space Science **307**(1-3): 57-62.

Cudworth, K. M. and Herbig, G. (1979). "2 Large Proper-Motion Herbig-Haro Objects." Astronomical Journal **84**(4): 548-551.

Dalgarno, A. and McCray, R. A. (1972). "Heating and Ionization of Hi Regions." Annual Review of Astronomy and Astrophysics **10**: 375-&.

Devine, D., Bally, J., Reipurth, B., Stocke, J. and Morse, J. (2000). "Hubble Space Telescope Planetary Camera imaging of HH 29." Astrophysical Journal **540**(1): L57-L59.

Devine, D., Reipurth, B. and Bally, J. (1999). "L1551 NE or L1551 IRS 5: Which source drives HH 28/29?" Astronomical Journal **118**(2): 972-982.

Elias, J. H. (1978). "Study of Taurus Dark Cloud Complex." Astrophysical Journal **224**(3): 857-872.

Emerson, J. P., Harris, S., Jennings, R. E., Beichman, C. A., Baud, B., Beintema, D. A., Marsden, P. L. and Wesselius, P. R. (1984). "Iras Observations near Young Objects with Bipolar Outflows - L1551 and Hh 46-47." Astrophysical Journal **278**(1): L49-L52.

Ferreira, J., Dougados, C. and Cabrit, S. (2006). "Which jet launching mechanism(s) in T Tauri stars?" Astronomy & Astrophysics **453**(3): 785-796.

Fridlund, C. V. M., Liseau, R. and Perryman, M. A. C. (1993). "High-Resolution Spectrophotometric Imaging of the Herbig-Haro Object Hh-29 in the L-1551 Outflow." Astronomy and Astrophysics **273**(2): 601-610.

Haro, G. (1952). "Herbig Nebulous Objects near Ngc 1999." Astrophysical Journal **115**(3): 572-&.

Haro, G. (1953). "Ha Emission Stars and Peculiar Objects in the Region of the Orion Nebula." Astrophysical Journal **117**(1): 73-&.

Hartigan, P. (1989). "The Visibility of the Mach Disk and the Bow Shock of a Stellar Jet." Astrophysical Journal **339**(2): 987-999.

Hartigan, P. (2003). "Shockwaves in outflows from young stars." Astrophysics and Space Science **287**(1-4): 111-122.

Hartigan, P., Foster, J. M., Wilde, B. H., Coker, R. F., Rosen, P. A., Hansen, J. F., Blue, B. E., Williams, R. J. R., Carver, R. and Frank, A. (2009). "Laboratory Experiments, Numerical Simulations, and Astronomical Observations of Deflected Supersonic Jets: Application to Hh 110." Astrophysical Journal **705**(1): 1073-1094.

Hartigan, P. and Morse, J. (2007). "Collimation, Proper Motions, and Physical Conditions in the HH 30 Jet From Hubble Space Telescope Slitless Spectroscopy." Astrophysical Journal **660**: 426-440.

Hartigan, P., Morse, J., Palunas, P., Bally, J. and Devine, D. (2000). "Kinematics of Herbig-Haro objects in the protostellar outflow L1551 as mapped by Fabry-Perot spectroscopy." Astronomical Journal **119**(4): 1872-1880.

Hartigan, P., Raymond, J. and Hartmann, L. (1987). "Radiative Bow Shock-Models of Herbig-Haro Objects." Astrophysical Journal **316**(1): 323-348.

Herbig, G. H. (1950). "The Spectrum of the Nebulosity Surrounding T-Tauri." Astrophysical Journal **111**(1): 11-&.

Herbig, G. H. (1951). "The Spectra of 2 Nebulous Objects near Ngc-1999." Astrophysical Journal **113**(3): 697-&.

Landau, L. D. and Lifshitz, E. M. (1987). Fluid mechanics. Oxford, England ; New York, Pergamon Press.

Mazzotta, P., Mazzitelli, G., Colafrancesco, S. and Vittorio, N. (1998). "Ionization balance for optically thin plasmas: Rate coefficients for all atoms and ions of the elements H to Ni." Astronomy & Astrophysics Supplement Series **133**(3): 403-409.

Osterbrock, D. E. and Ferland, G. J. (2006). Astrophysics of gaseous nebulae and active galactic nuclei. Sausalito, Calif., University Science Books.

Pudritz, R. E., Ouyed, R., Fendt, C. and Brandenburg, A. (2007). Disk Winds, Jets, and Outflows: Theoretical and Computational Foundations. Protostars and Planets V. B. Reipurth, D. Jewitt and K. Keil. Tucson, University of Arizona Press.

Raga, A.C., de Gouveia Dal Pino, E.M., Noriega-Crespo, A., Mininni, P.D. and Velázquez, P.F. (2002). "Jet/cloud Collision, 3D Gasdynamic Simulations of HH 110." Astronomy & Astrophysics **392**: 267-276

Raymond, J. C. (1979). "Shock-Waves in the Inter-Stellar Medium." Astrophysical Journal Supplement Series **39**(1): 1-27.

Reipurth, B. and Bally, J. (2001). "Herbig-Haro flows: Probes of early stellar evolution." Annual Review of Astronomy and Astrophysics **39**: 403-455.

Reipurth, B., Yu, K. C., Heathcote, S., Bally, J. and Rodriguez, L. F. (2000). "Hubble Space Telescope NICMOS images of Herbig-Haro energy sources: [Fe II] jets, binarity, and envelope cavities." Astronomical Journal **120**(3): 1449-1466.

Rosen, P. A., Foster, J. M., Wilde, B. H., Hartigan, P., Blue, B. E., Hansen, J. F., Sorce, C., Williams, R. J. R., Coker, R. and Frank, A. (2009). "Laboratory experiments to study supersonic astrophysical flows interacting with clumpy environments." Astrophysics and Space Science **322**(1-4): 101-105.

Ryutov, D., Drake, R. P., Kane, J., Liang, E., Remington, B. A. and Wood-Vasey, W. M. (1999). "Similarity criteria for the laboratory simulation of supernova hydrodynamics." Astrophysical Journal **518**(2): 821-832.

Shang, H., Li, Z. and Hirano, N. (2007). Jets and Bipolar Outflows from Young Stars: Theory and Observational Tests. Protostars and Planets V. B. Reipurth, D. Jewitt and K. Keil. Tucson, The University of Arizona Press.

Shu, F. H., Najita, J. R., Shang, H. and Li, Z.-Y. (2000). X-Winds: Theory and Observations. Protostars and Planets IV. V. Mannings and e. al. Tucson, University of Arizona Press.

Stocke, J. T., Hartigan, P. M., Strom, S. E., Strom, K. M., Anderson, E. R., Hartmann, L. W. and Kenyon, S. J. (1988). "A Detailed Study of the Lynds-1551 Star Formation Region." Astrophysical Journal Supplement Series **68**(2): 229-&.

Tsinganos, K. C., Ray, T. P. and Stute, M., Eds. (2009). Protostellar jets in context. Astrophysics and space science proceedings. Berlin ; New York, Springer.

Verner, D. A. and Ferland, G. J. (1996). "Atomic data for astrophysics .1. Radiative recombination rates for H-like, He-like, Li-like, and Na-like ions over a broad range of temperature." Astrophysical Journal Supplement Series **103**(2): 467-473.

Yirak, K., Frank, A. and Cunningham, A. J. (2010). "Self-Convergence of Radiatively Cooling Clumps in the Interstellar Medium." Astrophysical Journal **722**(1): 412-424.